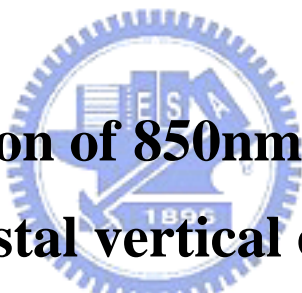


國立交通大學
光電工程研究所

碩士論文

850nm 高速和光子晶體面射型雷射之特性量
測與分析



**Characterization of 850nm high speed and
photonic crystal vertical cavity surface
emitting lasers**

研究生：曾國峰

指導教授：郭浩中教授

中華民國九十四年六月

850nm 高速和光子晶體面射型雷射之特性量測與分析

Characterization of 850nm high speed and photonic crystal

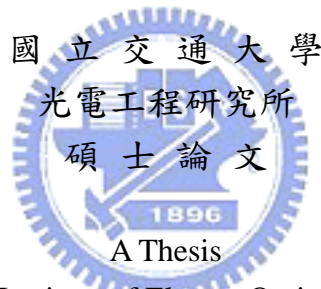
vertical cavity surface emitting lasers

研究生:曾國峰

Student : Kuo-Feng Tzeng

指導教授:郭浩中 教授

Advisor : Hao-Chung Kuo



Submitted to Institute of Electro-Optical Engineering
College of Electrical Engineering and Computer Science
National Chiao Tung University
in Partial Fulfillment of the Requirements
for the Degree of
Master
In

Electro-Optical Engineering

June 2005

Hsinchu, Taiwan, Republic of China

中華民國 九十四 年 六 月

Characterization of 850nm high speed and photonic crystal vertical cavity surface emitting lasers

Student: Kuo-feng Tseng

Advisors: Dr. Hao-Chung Kuo

Institute of Electro-Optical Engineering
National Chiao Tung University

Abstract

This thesis presents our study on GaAs based vertical-cavity surface-emitting laser (VCSEL) and is divided into two parts. The first part discuss the improvement of high speed performance of oxide VCSEL by utilizing tapered oxide layer.

We setup wafer-level high speed measurement system which allows us to test device immediately and avoids parasitic effect from package. The damping rate from the modulation response was found to reduce two times in the tapered oxide VCSEL and therefore enhanced the maximal modulation bandwidth. With same oxide aperture size 5.5 μm , tapered oxide VCSEL shows better modulation bandwidth of 13.2 GHz while blunt oxide VCSEL has 9.5 GHz. A very clean eye was demonstrated from improved VCSEL with rising time of 26 ps, falling time of 40 ps and jitter of less than 20 ps, operating at 10Gb/s with 6mA bias and 6dB extinction ratio. We also build an equivalent circuit model to analyze the bandwidth limitation affected by VCSEL intrinsic impedance. The simulation results could make the modulation limitation clearly and help us to modify the VCSEL process for high speed operation.

In the second part of the thesis, we report a high power (>1 mW) singlemode proton-implanted photonic crystal vertical-cavity surface-emitting laser (PC-VCSEL) with high SMSR (> 40 dB) throughout the whole operation current range. This PC-VCSEL, with an aperture of about 10 μm , has ultra-low threshold current of about 1.25 mA. We analyze the L-I curve, emission spectra, near field pattern, divergence angles of photonic crystal VCSELs fabricated with oxide-confined and implant

structure. The present results indicate that a VCSEL using proton implantation for current confinement and photonic crystal for optical confinement is a reliable approach to achieve high-power singlemode operation of a VCSEL. This concept will be applied to a 1.3 μm VCSEL and other commercial applications in the future.



850nm 高速和光子晶體面射型雷射之特性分析

研究生:曾國峰

指導教授:郭浩中 教授

交通大學光電工程研究所

摘要

本論文針對砷化鎵之面射型雷射(VCSEL)分成兩部分來探討，第一部分對於面射型雷射(VCSEL)在進行離子佈植製程後，對於不同氧化層之氧化型面射型雷射高速特性影響進行研究分析，並逐一建立元件結構之等效電路模型來進行模擬比對，第二部分對於氧化型和離子佈植型的光子晶體面射型雷射(VCSEL)，從光子晶體雷射的L-I曲線、輸出頻譜、近場發光圖形以及發散角等對光子晶體雷射做詳細的探討。

研究的850nm VCSEL，其磊晶結構為上及下反射層分別由22及39層 $\text{Al}_{0.15}\text{Ga}_{0.85}\text{As}$ / $\text{Al}_{0.9}\text{Ga}_{0.1}\text{As}$ 構成，主動層為GaAs / AlGaAs多重量子井，氧化層 $\text{Al}_{0.98}\text{Ga}_{0.02}\text{As}$ 成長於主動層上三層處。在高速特性量測方面，完成建立兩晶圓級之量測系統，可在製程之後直接點測元件的高速特性，以避免封裝對於元件造成調變速度限制。

首先我們探討尖細型氧化層讓電流孔徑小於輸出光孔徑而且也讓衰減率也進而變小兩倍進而提升調變速度。論文首先以普遍製作高速元件之氧化型VCSEL一比較實驗。實驗量測結果顯示，在同樣氧化孔徑 $5.5\ \mu\text{m}$ 下，一般氧化結構之VCSEL與尖細型氧化結構之VCSEL，其調變速度分別為9.5及13.2 GHz。接著尖細型氧化結構之VCSEL擁有清晰的眼狀圖(eye diagram)其下降時間為26 ps, 上升時間為40 ps 而抖動也小於20 ps。

接著根據不同的VCSEL結構，建立一等效電路模型，以Agilent ADS程式進行模擬，分析元件結構中等效RC對高速調變的影響。由等效電路的分析模擬，可以更清楚瞭解元件結構影響高速特性的程度，進而改進元件製程，以期能製造出更高速的VCSEL。

最後我們探討(邊模抑制比SMSR) $>40\text{dB}$ 之高輸出功率($>1\ \text{mW}$)單一模態離子佈植光子晶體面射型雷射(PC-VCSEL)。此光子晶體面射型雷射擁有非常低的臨界電流為1.25mA，其氧化孔徑為 $10\ \mu\text{m}$ 。由實驗結果可知，使用離子佈植當作電流侷限和光子晶體當作輸出光侷限可製作出高輸出功率單一模態的面射型雷射。而相同的概念也將會在未來逐漸被應用在 $1.3\ \mu\text{m}$ 面射型雷射上。

誌謝

Acknowledgements

隨著時間的車輪邁進，碩士生涯終於來到了終點，儘管那黃金似的日子是一去不復返的，但那黃金似的情誼却將永遠閃爍著光芒。感謝王興宗老師、郭浩中老師的提攜扶持、救危解困，若沒有您們的協助，這本論文便無法順利完成，內心的感謝是千言萬語也無法傳達其中一二，請原諒我僅以一聲：「謝謝」回報您們。

在此要特別感謝張亞銜學長，在過去一年半的時間裡，從實驗的建立，一直到完成研究這過程的指導及協助，並一起解決實驗上所遇到的各種問題。另外，也非常感謝道鴻學長在論文撰寫上的指教，芳儀學姐在儀器操作上的指導，以及彭朋群學長、姚忻宏學長和張詒安學長在研究方面適時地解決我的疑惑，有時真懷疑你們是不是上天派來的天使，總是恰如其份的推我一把，你們雪中送來的柴火至今仍在在我心中散發溫暖地燒著。

除此之外，尚有一干好友使我在研究生涯之外平添許多樂趣，裕鈞、敏瑛、永昌、瑞溢、文燈、蕙婷及傳煜，有些在我做實驗的當中陪我聊天解悶，有些在平凡的日子中陪我談笑遊玩，容忍我突如其來的痴狂，有些更是陪我踏上新竹的好山好水，領略人生的優美與曲折，若是少了你們的生氣，碩士生涯就不會這麼的令人不捨及動人，很高興有你們的陪伴。還有碩一的學弟妹文凱、意偵、伯傑、宗鼎、剛帆、游敏、志堯及皇申，謝謝你們的幫忙，跟你們相處非常的愉快。

不能或忘的，是父親、母親的關懷體貼，若沒有您們的支持，我也不能無後顧之憂的將大片的青春揮霍，讓年輕的笑顏展放在大學校園，十多年的栽培令我深深受用，而今我將踏出校園，反哺您們的教養之恩。當然，琬萍的鼓勵與支持是功不可沒的。尤其在繁忙的課業壓力下，沒有妳的悉心照料與包容，肯定是無法順利完成論文。

兩年的研究生涯一晃眼就過了，卻留下滿滿的回憶，載不走的，載不走的，也要使盡力氣扛著，因為不是你們點綴我的生活，而是我點綴了你們的生活，讓日子發光發亮的，是諸位親愛的師友啊。很愉快能有這麼暢快的學生生活，既使我將在這兒劃下暫離的句點，諸位在交大校園的身影我會謹記於心的。

Content

List of Tables.....	V
List of Figures.....	VI
Chapter 1 Introduction and overview.....	1
1.1 VCSEL review.....	1
1.2 Fundamental of VCSEL.....	2
1.3 Develop trend and future.....	3
1.4 Applications of VCSELS.....	4
1.4.1 Data communication.....	4
1.4.2 Optical interconnect.....	5
Chapter 2 Theory.....	12
2.1 Recombination mechanism of multi-quantum-well.....	12
2.2 Transfer function.....	15
2.3 V-parameter.....	18
Chapter 3 VCSEL fabrication and measurement setup.....	26
3.1 Fabrication of tapered and blunt oxide VCSEL	26
3.2 Fabrication of photonic crystal VCSEL.....	27
3.2.1 Fabrication of oxide photonic crystal VCSEL	27
3.2.2 Fabrication of implant photonic crystal VCSEL.....	28
3.3 Probe station and spectrum measurement system.....	28
3.4 Far field pattern measurement system.....	29
3.5 Microwave test and eye diagram measurement system.....	29
3.6 Experimental guidelines.....	30

Chapter 4 Result and Discussion.....	40
4.1 Oxide-implant VCSELs DC and AC characteristics.....	40
4.2 Equivalent circuit modeling.....	42
4.3 photonic crystal VCSELs DC characteristics.....	43
Chapter 5 Conclusion.....	56
Reference.....	57



List of Tables

Table 1-1 Comparison of parameters between stripe laser and VCSEL.....	11
Table 4-1 Equivalent circuit elements at different bias current for Tapered oxide VCSEL.....	55



List of Figures

Figure 1-1 Comparison Sketch of edge-emitting laser and VCSEL.....	1
Figure 1-2 A modal of vertical cavity surface emitting laser (VCSEL).....	7
Figure 1-3 Material for VCSELs in wide spectral bands.....	7
Figure 1-4 Structure for current confinement for VCSELs.....	8
Figure 1-5 Global consumption value of diode laser by the year 2002.....	8
Figure 1-6 Global consumption value of diode by the year 2002.....	9
(distinguished into wavelength).....	9
Figure 1-7 Transmission spectrum for silica fiber.....	10
Figure 1-8 12 channel 2.5 Gb/s VCSEL array for short distance transmission applications.....	4
Figure 2-1 Band diagram of active region of VCSEL.....	21
Figure 2-2 Reservoir analogy (a) under threshold (b) above threshold.....	22
Figure 2-3 Basic electronic recombination/generation mechanism.....	23
Figure 2-4 Schematic of VCSEL illustrating active region and cavity volumes.....	24
Figure 2-5 Conversion from electrical small signal train into optical signal.....	24
Figure 2-6 Small signal modulation response of a VCSEL.....	25
Figure 3-1 Cross section structure of tapered oxide implant VCSEL structure.....	32
Figure 3-2 Steps of oxide-implant VCSEL process.....	33
Figure 3-3 Illustration of oxidation process system setup.....	34
Figure 3-4 Oxidation rate of 98% Al-content layer.....	34
Figure 3-5 (a) Cross section structure of oxide photonic crystal VCSEL structure (b) top view image of the PC-VCSEL;(c) scanning electron microscope image of an etched hole.....	35
Figure 3-6 Steps of oxide photonic crystal VCSEL process.....	36
Figure 3-7 Cross section structure of implant photonic crystal VCSEL.....	37
Figure 3-8 Probe station measurement instrument setup.....	38
Figure 3-9 Far field pattern measurement system.....	38
Figure 3-10 eye diagram measurement instrument setup.....	39
Figure 4-1 Tapered oxide and blunt oxide VCSEL structure.....	45
Figure 4-2 Typical LIV curve for tapered oxide and blunt oxide VCSELs.....	45
Figure 4-3 Modulation responses for both tapered oxide and Blunt oxide VCSELs...	46

Figure 4-4 Resonance and 3dB frequency as a function of $(I-I_{th})^{1/2}$ for oxide-only and oxide-implant VCSELS.....	47
Figure 4-5 damping rate as a function of square of resonant frequency for tapered oxide and blunt oxide VCSELS.....	47
Figure 4-6 Real and imaginary S11 parameter versus frequency from model and measured data (dash line is measured data, solid line is simulated data)	48
Figure 4-7 Eye-diagram for tapered oxide and blunt oxide VCSELS.....	49
Figure 4-8 oxide VCSEL and oxide photonic crystal VCSEL structure.....	50
Figure 4-9 Typical LIV curve for oxide photonic crystal VCSELS.....	51
Figure 4-10 Spectral characteristics and near-field images for the photonic crystal VCSELS.....	51
Figure 4-11 Implant photonic crystal VCSEL.....	52
Figure 4-12 Typical LIV curve for implant photonic crystal VCSELS.....	52
Figure 4-13 Spectral characteristics for the implant photonic crystal VCSELS and VCSEL without PC holes (a) PC-VCSEL (b)VCSEL	53
Figure 4-14 Far field patterns of the fimplant VCSELS observed under different drive currents are shown in (a)~(c) and the implant photonic crystal VCSEL are shown in (d)~(f).....	54
Figure 4-15 The divergence angle for implant and photonic crystal VCSELS.....	54

Chapter 1

Introduction and overview

1.1 Review of VCSEL

Vertical cavity surface emitting lasers (VCSELs) was first demonstrated in 1979 by H. Soda, K. Iga, F. Koyama and S. Kinoshita [1]. While the cavity design was novel as compared to the established edge-emitting lasers, the initial device performance was poor in terms of the high threshold current density and low output power that it apparently attracted little attention. Continued work by Iga and various coworkers, however, showed continuous improvements in performance, eventually leading to the first continuous wave VCSEL operation, at room temperature, reported in 1988 [2]. By that time other important innovations and demonstrations had brought growing attention to the VCSEL. Figure 1-1 shows the comparison sketch of edge-emitting laser and VCSEL.

The VCSEL structure may provide a number of advantages over traditional lasers, as follow:

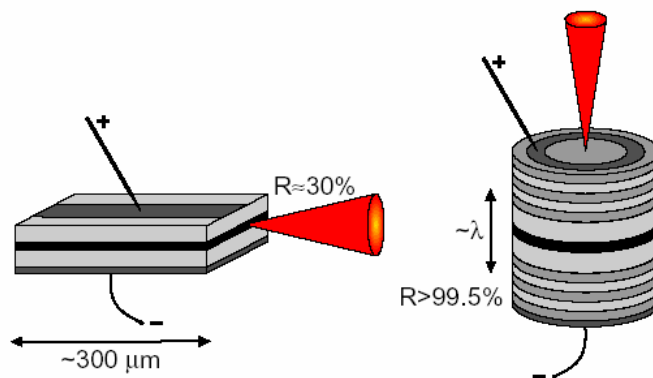


Figure 1-1 Comparison Sketch of edge-emitting laser and VCSEL

- ▲ Low threshold operation for its small cavity volume
- ▲ High-speed modulation capability
- ▲ Low power consumption
- ▲ Low cost chip production
- ▲ Vertical emission from the substrate
- ▲ Easy coupling to optical fiber due to circular beam
- ▲ The initial probe test can be performed before separating device into discrete

chips

- ▲ Densely packed and precisely arranged two-dimensional laser arrays
- ▲ Higher reliability
- ▲ Higher integration

The progress of the vertical cavity surface emitting laser in the late 1990s was very fast, and various applications to optoelectronics [3]. In 1992, VCSELs based on GaAs have been extensively studied some of the 0.98, 0.85 and 0.78 μm wavelength devices are now commercialized into optical system. VCSELs are currently to be the ideal laser source for fiber optic application.

1.2 Fundamental of VCSEL

The structure common to most VCSELs consists of two parallel reflectors which sandwich a thin active layer, is illustrated with Figure 1-2. The reflectivity necessary to reach the lasing threshold should normally be higher than 99.9%. Together with the optical cavity formation, the scheme for injecting electrons and holes effectively into the small volume of the active region is necessary for a current injection device. The ultimate threshold current depends on how to make the active volume small and how well the optical field can be confined in the cavity to maximize the overlap with the active region. These confinement structures will be presented later.

There are some choices of the materials for semiconductor lasers in Figure 1-3. The availability of substrates against lattice constant related to the systems is also shown. The problems are listed below that should be taken into account consideration for making VCSELs:

- ▲ Design of resonant cavity and mode-gain matching
- ▲ Multi-layered distributed Bragg reflectors (DBRs) to realize high-reflective mirrors
- ▲ Heat sinking for high temperature and high power operation

In addition, the resistivity of material is crucial for high speed operation.

These are typical methods of current confinement schemes for the VCSEL structures, indicated in Figure 1-4, reported so far.

- ▲ Ring electrode type: This structure can limit the current flow in the vicinity of the ring electrode. The light output can be taken out from the center window. This is easy to fabricate, but the current can not completely be confined to a small area due to diffusion.
- ▲ Proton-implant type: An insulating layer made by proton (H^+) irradiation to limit the current spreading toward the surrounding area. The process is rather simple and most commercialized devices are made by this method.
- ▲ Regrowth Buried-Heterostructure (BH) type: The mesa etching including active region form a wide-gap semiconductor to limit the current. The refractive index can be small in the surrounding region, resulting in forming an index-guiding structure. This is one of ideal structures in terms of current and optical confinement. The problem is that the necessary process is rather complicated.
- ▲ Air-post type: The circular or rectangular air post is used to achieve a current confinement. It is the simplest method of device fabrication, but non-radiative recombination at the outer wall may reduce the performance.
- ▲ Selective AIAs oxidation type: By oxidizing the AIAs layer to form an insulator.

By developing new process technology could achieve the better laser performance.

1.3 Development trend

The market forecast of 2002 global laser diode market analysis [4], indicated in Figure 1-5, appears that optical communication and storage have almost 84% market demand. Moreover, the market distinguished into wavelength, Figure 1-6, shows 780~980nm laser diode in chief. For telecommunication, development of Ethernet causes the needs of capacity increasing rapidly. Metro-area network (MAN) would use fiber optical communication replace traditional cable to satisfy high-capacity requirement. Local-area network (LAN) would expand fiber to the home (FTTH) which developed rapidly in Japan now. Primary transmission rate is developed almost up to 10Gbps suitable for OC-192 standard by ANSI [5]. Storage-area network (SAN), another major growth sector, perhaps is the brightest spot in networking. These interconnections link large disk arrays to servers and other systems. The reigning technology is Fiber Channel (FC), an optical ring configuration

that has become the standard. FC continues to get faster as the newer versions of the standard have increased rates to 1.0625 Mbits/s and 2.125 Gbits/s, making this system even more desirable today. Faster 4G and 10G systems are in the works.

VCSEL with advantage of wide-band and small-volume transmission capability is an appropriate laser source for those applications. Long wavelength VCSELs provide ultimate transmission capacity in long-distance; 850nm VCSELs are suited to short-distance communication such as LAN. VCSELs contain primary fiber optic communication channels, that is, 850/1310/1550nm which has less attenuation in fiber link, indicated in Figure 1-7. Beside of communication, the high-speed demand for optical storage is growth. International associate precisely define 650nm laser as beam recorder. VCSELs almost contain wide-band transmission application.

1.4 Applications of VCSELs

1.4.1 Data communication

Today, datacom moduels based on near-infrared VCSELs represent 95% of the VCSEL market, 80% of which are commercialized by a few companies: Agilent, Honeywell, Infineon, Furukawa and Zarlink. The remaining 20% are shared among numerous start-ups offering innovative designs. The market has recently exploded: it is evaluated to be worth USD 500 million at present, and is constantly growing due to the rapid deployment of Gigabit Ethernet and fiber channels. Most of today's commercial datacom components are based on oxide 850 nm VCSELs. They are often package as single component or in

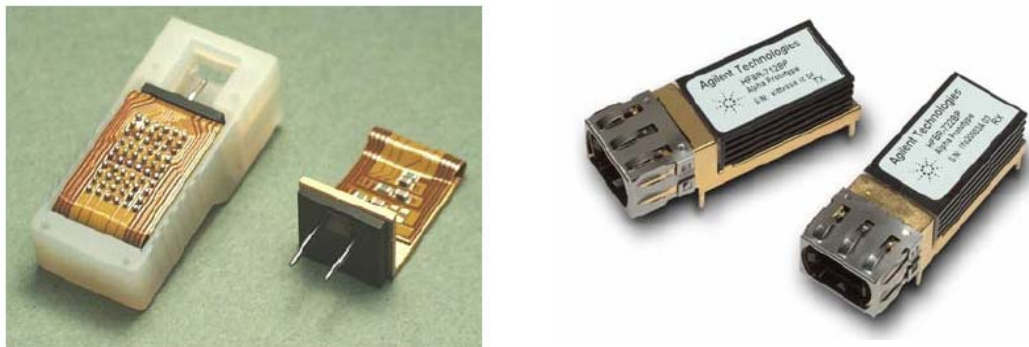


Figure 1-8 12 channel 2.5 Gb/s VCSEL array for short distance transmission applications.

parallel fiber modules of linear arrays, offering 4 to 12 channels at 2.6 GB/s per channel, which aggregate bandwidth up to 30 GB/s. The research and development efforts are focusing on the next generation of high speed VCSEL, and a number of groups have reported transmission at 10 GB/s or more for distances up to 300 m of MMF. [Figure 1-8](#) shows a 12 channel 2.5 Gb/s VCSEL array for short distance transmission applications.

For long wavelength part, Metro and Access Networks are dominated by 1300nm and 1550 nm FP and DFB lasers up to now. A long wavelength VCSEL (LW-VCSEL) would be an ideal low-cost alternative to the DFB laser, particularly for the standard IEEE 802.3ae applications, which extend the existing Gigabit Ethernet into traditional SONET markets at OC-192 data rates. However, the performance specifications for such LW-VCSELs are challenging. For low-cost transceivers, they must operate over the 0 to 70 C temperature range for indoor applications and over the -40 to 85 C range for outdoor applications, without external temperature stabilization. The laser power launched into the single mode fiber must usually be more than 0.7 mW in order to support transmission distance of 10 km at 10 GB/s. Despite intense research effort, the technology so far has not yet met these requirements.

1.4.2 Optical interconnect

The optical interconnect is considered to be inevitable in the computer technology. The performance of massively parallel computers is usually limited by the communication bottleneck between processors. Optic provides an effective mean to line these processors because of its high capacity, low crosstalk and attenuation, and the possibility to obtain three-dimensional architectures. Other potential applications include routers, switches and storage. The VCSEL is a strong candidate as the preferred optical light source for the emerging optical interconnect mass market, meeting the requirement of low cost, high density integration and low power dissipation. A 256-channel bi-directional optical interconnect using VCSELs and photodiodes on CMOS was demonstrated.

The mainstream of commercial high-speed VCSEL is 2.5Gbps (OC-48) and few

laboratories and corporations research in 10Gbps device, as [Table1-1](#). In this paper, we focus on high-speed 850nm vertical cavity surface emitting lasers. First, we mention major VCSEL structure process, oxide and oxide-implantation, and explain high-speed test system in detail in chapter 2. In chapter 3, a simple introduction of phenomenon approach the rate equation is presented. The scattering coefficients are estimated by high-speed measurement, Transfer function is used in analyzing dynamic characteristics as relaxation frequency, damping rate. We measure static and dynamic characteristics of VCSELs and create an equivalent circuit for modeling in chapter 4. Finally, we give a brief conclusion in chapter 5.



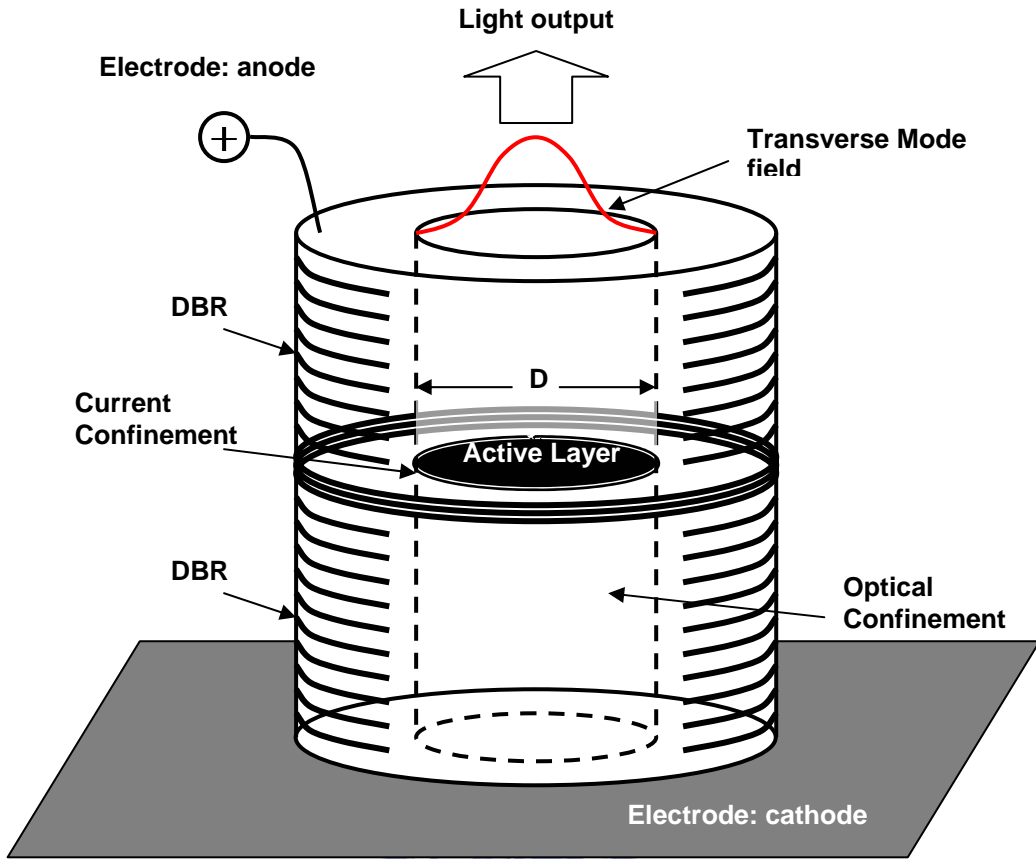


Figure 1-2 A modal of vertical cavity surface emitting laser (VCSEL)

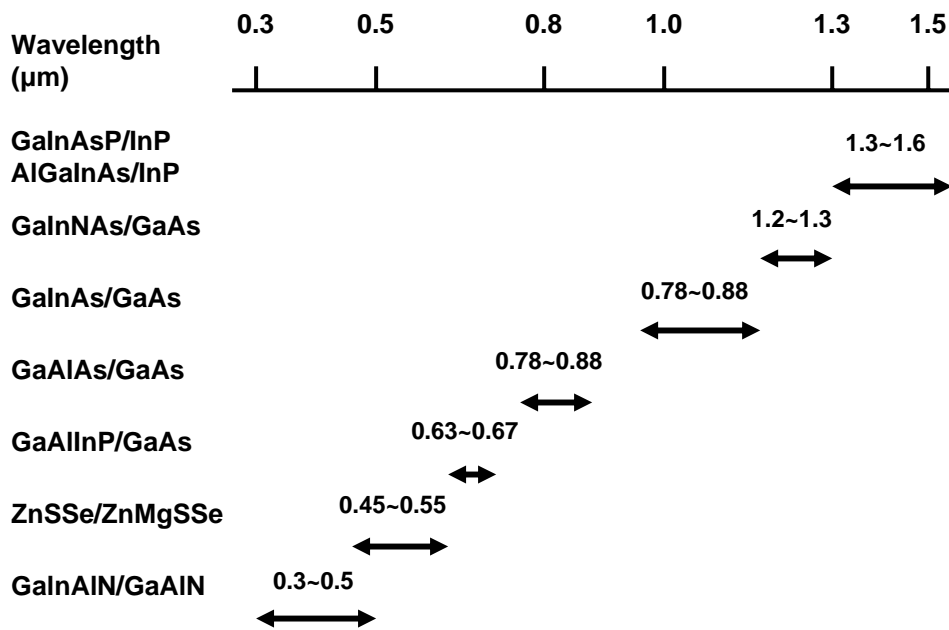


Figure 1-3 Material for VCSELs in wide spectral bands

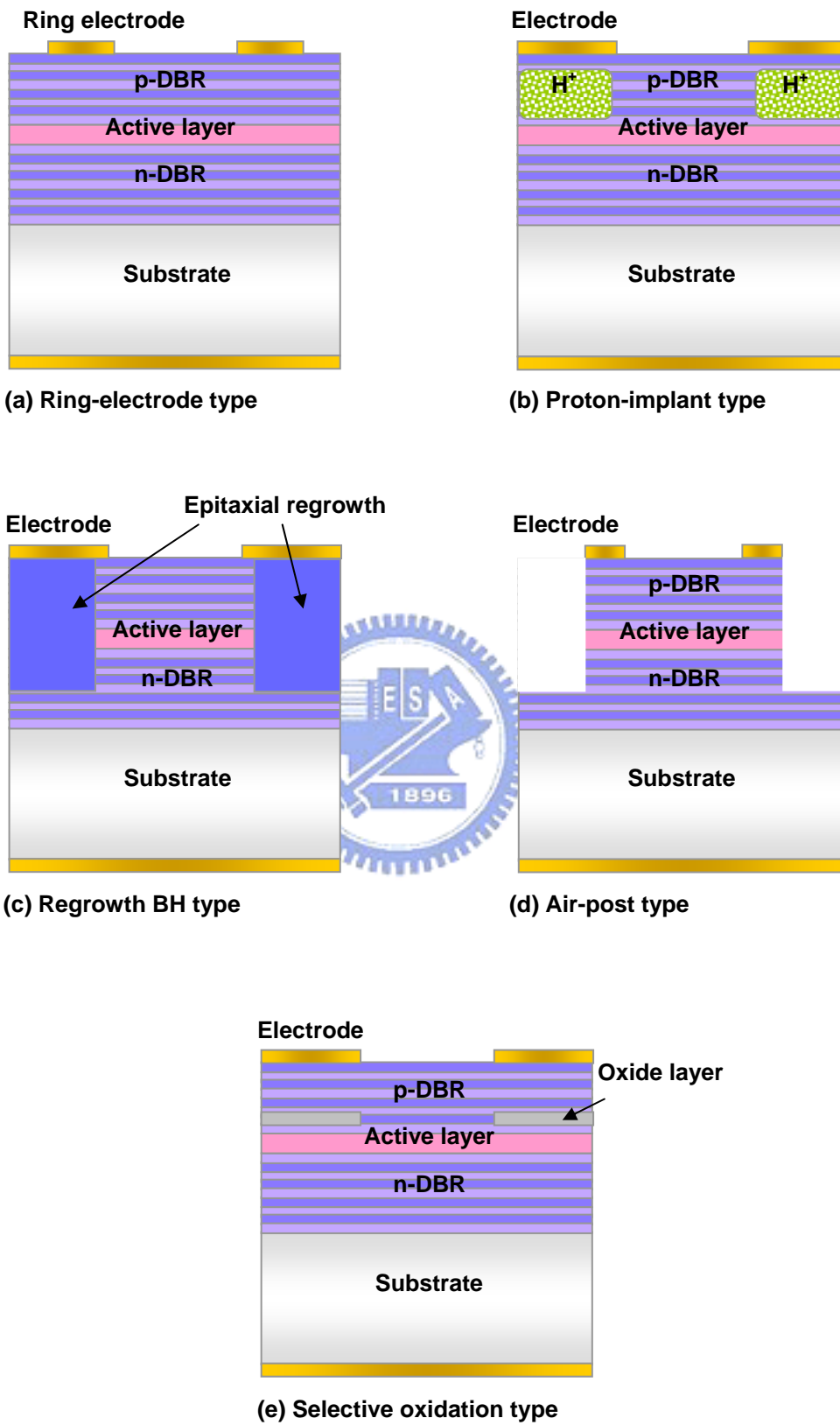


Figure 1-4 Structure for current confinement for VCSELs

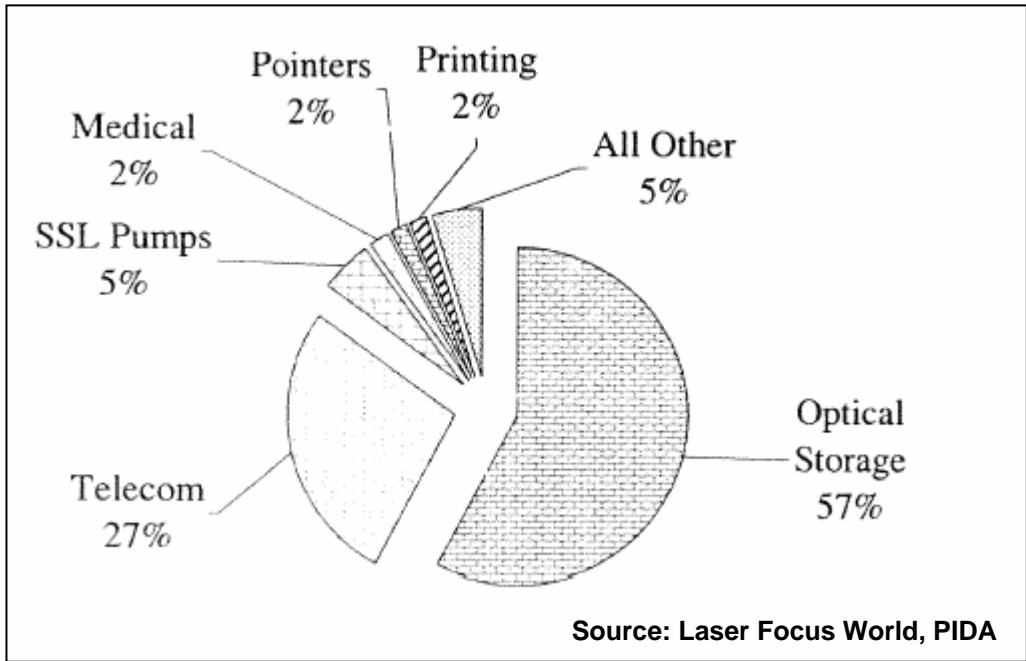


Figure 1-5 Global consumption value of diode laser by the year 2002

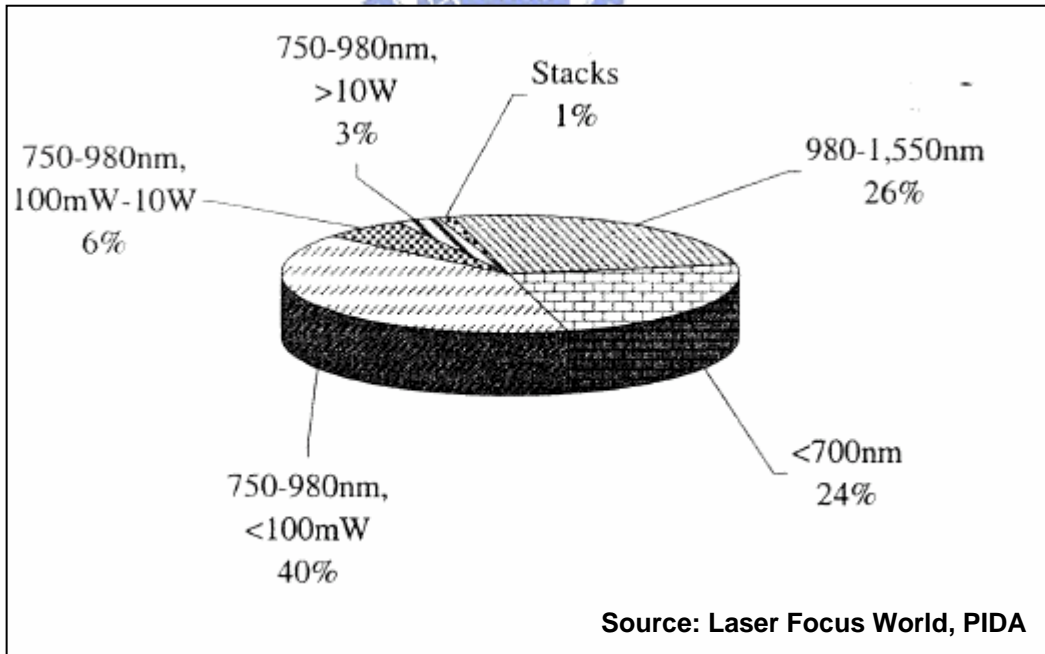


Figure 1-6 Global consumption value of diode by the year 2002 (distinguished into wavelength)

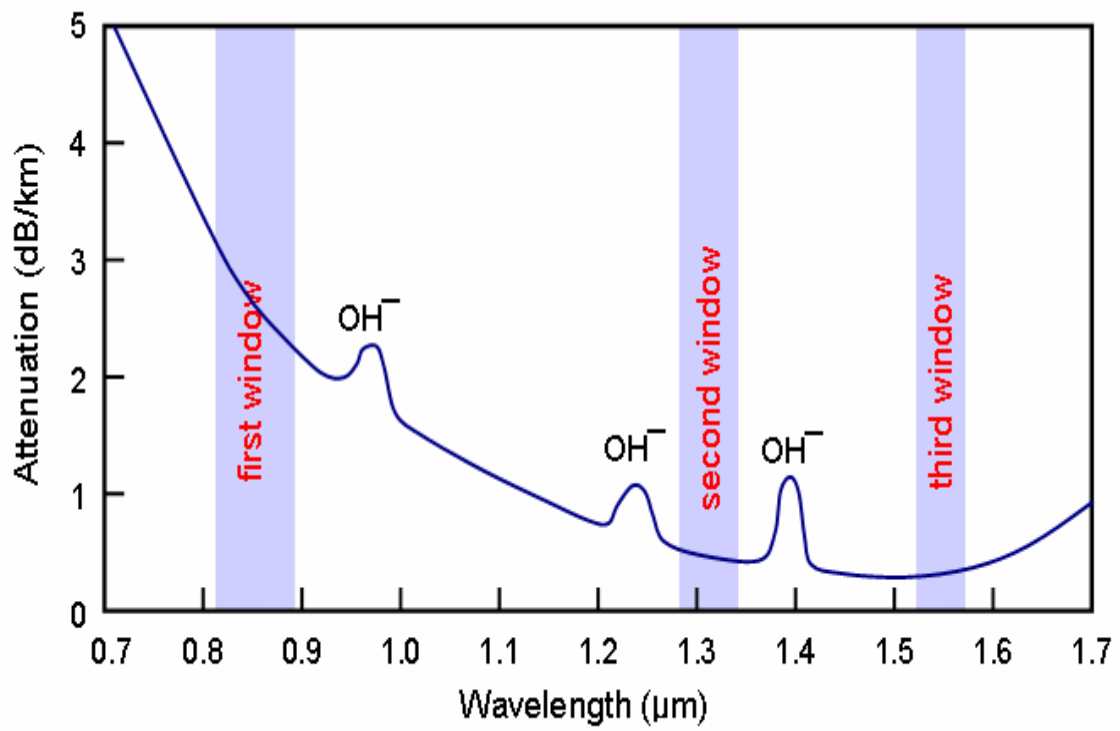


Figure 1-7 Transmission spectrum for silica fiber

Parameter	Symbol	Material	Wavelength
Active layer thickness	d	100 Å ~ 0.1μm	80 Å ~ 0.5μm
Active layer area	S	3 x 300 μm ²	5x5μm ²
Active volume	V	60 μm ³	0.07μm ³
Cavity length	L	300 μm	~1 μm
Reflectivity	R _m	0.3	0.99 – 0.999
Optical confinement	ξ	~ 3 %	~ 4 %
Optical confinement (Transverse)	ξ _t	3 – 5 %	50 – 80 %
Optical confinement (Longitudinal)	ξ _l	50 %	2 x 1% x 3 (3 QWs)
Photon Life time	τ _p	~ 1 ps	~ 1 ps
Relaxation Frequency (Low Current Levels)	f _r	< 5 GHz	> 10 GHz

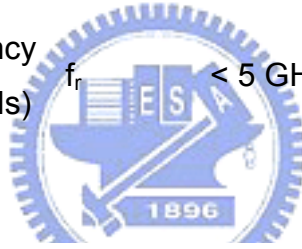


Table 1-1 Comparison of parameters between stripe laser and VCSEL

Chapter 2

Theory

The chapter begins by developing a reservoir model for a flow of charge into double-heterostructure active regions and its subsequent recombination. Recombination mechanism is determined by electron-hole recombination at quantum well generates photons for light emission. For this we describe the phenomenological approach to VCSEL first.

The rate equations provide the most fundamental description of the laser in next section. It describes the time-evolution of carrier and photon densities in a laser cavity as a function of the pump rate, material gain and parameters associated with the material properties and laser construction. Dynamic characteristics of VCSEL are studied as rate equation, and it is produced for modulated current injection. Transfer function is relevant equation originated from rate equation which is explained next.

The last section is presented of V-parameter used in 2-D photonic crystal structure, the V-parameter evaluating the number of guided modes in cylindrical wave guides the rate equations for carriers and photons are found to be analogous to differential equations that describe the current and voltage in an RLC circuit. Scattering parameter offers not only response as bandwidth but reflection coefficient which mirrored equivalent RLC circuit. Establishment of equivalent circuit is purposed to be found the limitation of bandwidth for VCSEL structure and making terminal impedance matching easily.

2.1 Recombination mechanism of VCSEL

The proposition considers the current injected into VCSEL, and suggests it is desirable to have all of it contributes to electrons and holes which recombine in the active region. Since the definitions of the active region and the internal quantum efficiency, η_i , are so critical to further analysis. Active region, evolved into lowest band-gap region, is where recombining carriers contribute to photon emission. Band diagram of active region, includes separate confinement hetero-structure (SCH)

band-gap region, illustrated in [Figure 2-1](#). Internal quantum efficiency, η_i , is the fraction of terminal current that generates carriers in the active region. It is important to realize that includes all of the carriers that are injected into active region, not just carriers that recombine induce radiating at the desired transition energy.

The carrier density, n , in the active region is governed by a dynamic process. In fact, we could compare the process of a certain steady-state carrier density in the active region to that a reservoir analogy, which is being simultaneously filled and drained, in a certain water level. This is shown schematically in [Figure 2-2\(a\)](#). For the double heterostructure active region, the injected current provides a generation term and various radiative and nonradiative recombination processes as well as carrier leakage provides recombination term. Thus, rate equation is determined as

$$\frac{dn}{dt} = G_{gen} - R_{rec} \quad (2-1)$$

where G_{gen} is the rate of injected electrons and R_{rec} is the rate of recombining electrons per unit volume in the active region. There are $\eta_i I/q$ electrons per second being injected into the active region. V is the volume of the active region.

The recombination process is accompanied with spontaneous emission rate, R_{sp} , and a nonradiative recombination rate, R_{nr} , depicted in [Figure 2-3](#). Carrier leakage rate, R_l , must be occurred at the transverse and/or lateral potential barrier are not sufficiently high. A net stimulated combination, R_{st} , is including both stimulated absorption and emission. That is, an increased injection results in an increased output, R_{st} , but no increase in carrier density as water level illustrated in [Figure 2-2\(b\)](#). Total recombination rate is expressed as below

$$R_{rec} = R_{sp} + R_{nr} + R_l + R_{st} \quad (2-2)$$

where the first three terms on the right refer to the natural carrier decay processes. It is common to describe the natural decay processes by a carrier lifetime, τ . In the absence of photon generation term, the rate equation for carrier decay is, $dn/dt = n/\tau$, where $n/\tau = R_{sp} + R_{nr} + R_l$, by comparison to Eq. (2-2). Thus, the carrier rate equation in equivalent be expressed as

$$\frac{dn}{dt} = \frac{\eta_i I}{qV} - \frac{n}{\tau} - R_{st} \quad (2-3)$$

The net stimulated recombination rate, R_{st} , in generating photons as well as effect of the resonant cavity in storing photons is investigated additionally. A rate equation for the photon density, n_p , which includes the photon generation and loss terms are constructed analogous to carrier rate equation. The main photon generation term above threshold is R_{st} . Every time an electron-hole pair is stimulated to recombine, another photon is generated. However, as indicated in [Figure 2-4](#), the cavity volume occupied by photons, V_p , is usually larger than the active region volume occupied by electrons, V , the photon density generation rate will be $(V/V_p)R_{st}$ not just R_{st} . This electron-photon overlap factor, (V/V_p) , is generally referred to as the confinement factor, Γ .

Photon loss occurs within the cavity due to optical absorption and scattering out of the mode, and it also occurs at the output coupling mirror where a portion of the resonant mode is usefully coupled to some output medium. These losses could characterize by a photon lifetime, τ_p . The photon rate equation takes the form

$$\frac{dn_p}{dt} = \Gamma R_{st} + \Gamma \beta R_{sp} - \frac{n_p}{\tau_p} \quad (2-4)$$

where β is the spontaneous emission factor. For uniform coupling to all modes, β is just the number of spontaneous emission coupled into specific mode in the bandwidth of all spontaneous emission.

R_{st} represents the photon stimulated net electron-hole recombination which generates more photons. This is a gain process for photon. An increased photon is proportional to an increased injection carriers overflow the reservoir, which is critical condition to generate stimulated emission, shown in [Figure 2-3](#). The proportion is defined as gain coefficient, $g(n)$. That is,

$$g(n) = g_0(n - n_{tr}) = v_g a(n - n_{tr}) \quad (2-5)$$

Where a is the differential gain. The term of $a(n - n_{tr})$ is determined approximately to laser oscillation condition with regenerated amplifier approach due to multiple reflection, as shown in [Appendix \(1\)](#). n_{tr} is a transparency carrier density, and v_g is the

group velocity of the mode of interest including both material and waveguide dispersion. v_g still can be expressed as C/n_r , where C is 3×10^8 m/s and n_r is index of cavity medium. Thus R_{st} is replaced with $g(n)n_p$, and now the carrier and photon density rate equations can be written as

$$\frac{dn}{dt} = \frac{\eta_i I}{qV} - \frac{n}{\tau} - g(n)n_p \quad (2-6)$$

$$\frac{dn_p}{dt} = \Gamma g(n)n_p + \Gamma \beta R_{sp} - \frac{n_p}{\tau_p} \quad (2-7)$$

Equations (2-6) and (2-7) are two coupled equations that can be solved for the steady-state and dynamic responses of a diode laser in next section.

2.2 Transfer function

Under small signal modulation, the carrier and photon density rate equation, Eq. (2-6) and (2-7), are used to calculate relaxation resonance frequency and its relationship to laser modulation bandwidth.

Consider the application of an above-threshold DC current, I_0 , carried with a small AC current, I_m , to a diode laser. Illustration is, shown in [Figure 2-5](#), under basic L-I characteristics (Light output power versus current). The small modulation signal with some possible harmonics of the drive frequency, ω . Small signal approximation, assumes $I_m \ll I_0$ bias and spontaneous emission term, β , is neglected, is expressed as

$$I = I_0 + I_m(t) = I_0 + I_m(\omega)e^{j\omega t} \quad (2-8)$$

$$n = n_0 + n_m(t) = n_0 + n_m(\omega)e^{j\omega t}$$

$$n_p = n_{p0} + n_{pm}(t) = n_{p0} + n_{pm}(\omega)e^{j\omega t}$$

Before applying these to Eq. (2-6) and (2-7), the rate equation is rewritten for the gain. Assumption under DC current is sufficiently above threshold that the spontaneous emission can be neglected. Without loss of generality, we suppose full overlap between the active region and photon field, $\Gamma=1$; furthermore, internal quantum efficiency, η_i , is neglected. That is,

$$\frac{dn}{dt} = \frac{I}{qV} - \frac{n}{\tau} - g_0(n - n_{tr})n_p \quad (2-9)$$

$$\frac{dn_p}{dt} = g_0(n - n_{tr})n_p + \beta R_{sp} - \frac{n_p}{\tau_p} \quad (2-10)$$

substitute Eq. (2-8) into Eq. (2-9)

$$\begin{aligned} \frac{d(n_0 + n_m)}{dt} &= \frac{(I_0 + I_m)}{qV} - \left(\frac{n_0 + n_m}{\tau} \right) - g_0(n_0 + n_m - n_{tr})(n_{p0} + n_{pm}) \\ &= \left(\frac{I_0}{qV} - g_0(n_0 - n_{tr})n_{p0} - \frac{n_0}{\tau} \right) + \left(\frac{I_m}{qV} + g_0(n_0 - n_{tr})n_{pm} - g_0n_{p0}n_m - \frac{n_m}{\tau} \right) \end{aligned}$$

for this, it is similarly expressed modulation terms as

$$\frac{dn_m}{dt} = \frac{I_m}{qV} + g(n_0)n_{pm} - g_0n_{p0}n_m - \frac{n_m}{\tau} \quad (2-11)$$

$$\frac{dn_{pm}}{dt} = g_0n_{p0}n_m + g(n_0)n_{pm} - \frac{n_{pm}}{\tau_p} \quad (2-12)$$

The small signal terms in frequency domain of carrier and photon are given by

$$n_m(t) = n_m(\omega)e^{j\omega t}$$

$$n_{pm}(t) = n_{pm}(\omega)e^{j\omega t}$$

substitute into Eq. (2-11) and (2-12), the equations become

$$j\omega n_m(\omega)e^{j\omega t} = \frac{I_m(\omega)e^{j\omega t}}{qV} + g(n_0)n_{pm}(\omega)e^{j\omega t} - g_0n_{p0}n_m(\omega)e^{j\omega t} - \frac{n_m(\omega)e^{j\omega t}}{\tau}$$

Carrier modulation term in frequency domain is simplified as

$$j\omega n_m(\omega) = \frac{I_m(\omega)}{qV} + g(n_0)n_{pm}(\omega) - g_0n_{p0}n_m(\omega) - \frac{n_m(\omega)}{\tau}$$

$$\left(j\omega + g_0n_{p0} + \frac{1}{\tau} \right) n_m(\omega) = \frac{I_m(\omega)}{qV} + g(n_0)n_{pm}(\omega) \quad (2-13)$$

Photon modulation term in frequency domain is simplified as

$$j\omega n_{pm}(\omega) = g_0 n_{p0} n_m(\omega) + g(n_0) n_{pm}(\omega) - \frac{n_{pm}(\omega)}{\tau_p}$$

$$\left(j\omega - g(n_0) + \frac{1}{\tau_p} \right) n_{pm}(\omega) = g_0 n_{p0} n_m(\omega) \quad (2-14)$$

Solve for $n_m(\omega)$ and $n_{pm}(\omega)$ using Eq. (2-13) and (2-14), we obtain the frequency response of two arranged equations as below

$$n_m(\omega) = \left(\frac{j\omega}{j\omega\Omega - \omega^2 - \omega_r^2} \right) \left(\frac{I_m(\omega)}{qV} \right) \quad (2-15)$$

$$\text{where } n_{pm}(\omega) = \left(\frac{\tau_p \omega_r^2}{j\omega\Omega - \omega^2 - \omega_r^2} \right) \left(\frac{I_m(\omega)}{qV} \right) \quad (2-16)$$

$$\omega_r^2 = (2\pi \cdot f_r)^2 = \left(\frac{n_{p0}}{\tau_p} \right) g_0 \quad \dots \text{Relaxation frequency} \quad (2-17)$$

$$\Omega = \frac{1}{\tau} + n_{p0} g_0 \quad \dots \text{Damping constant (decay rate)} \quad (2-18)$$

With the Eq. (2-15) and (2-16) we observe the coupling between the small signal photon, n_{pm} , and carrier, n_m . Small signal carrier injection induces photon achieved oscillation. This phenomenon produces a natural resonance in the laser cavity which shows up the output power of the laser in response to sudden changes in the input current. The natural frequency of oscillation associated with this mutual dependence between n_m and n_{pm} . Modulation response is expanded the small signal modulation relationship to steady-state. From Eq. (2-15) and (2-16), the modulation response is denoted as

$$M(\omega) = \frac{n_{pm}(\omega)}{n_{pm}(0)} = \left| \frac{\frac{\tau_p \omega_r^2}{j\omega\Omega - \omega^2 - \omega_r^2}}{\frac{\tau_p \omega_r^2}{\omega_r^2}} \right| = \left| \frac{\omega_r^2}{j\omega\Omega - \omega^2 - \omega_r^2} \right| \quad (2-19)$$

The general behavior of $M(\omega)$ is shown in [Figure 2-6](#). Modulation bandwidth is determined as cutoff frequency, f_c , which is the position with half response written as

$$M(\omega_c) = \frac{1}{2} M(0) = \frac{1}{2} \frac{\omega_r^2}{\left[(\omega_c^2 - \omega_r^2)^2 + \omega_r^2 \Omega^2 \right]} = \frac{1}{2} \quad (2-20)$$

for $\omega_r^2 \Omega^2 \ll (\omega_c^2 - \omega_r^2)^2$, the cutoff frequency, ω_c , is approximated to $\sqrt{3} \omega_r$.

Transfer function, $H(\omega)$, is the identical term in Eq. (2-11) and (2-12) respectively obtained with Cramer's rule [3]. It is similar to modulation response, $M(\omega)$, describing the response of the laser intensity to small variations in the drive current through the active region. That is,

$$H(f) = C \frac{f_r^2}{f_r^2 - f^2 + j \frac{f}{2\pi} \gamma} \quad (2-21)$$

where f_r is the resonance frequency same as Eq. (2-17), γ is the damping rate similar to Eq. (2-18), and C is a constant. Accounting for additional extrinsic limitations due to carrier transport and parasitic elements related to the laser structure results in an extra pole in the small signal modulation transfer function

$$H(f) = C \left(\frac{f_r^2}{f_r^2 - f^2 + j \frac{f}{2\pi} \gamma} \right) \cdot \left(\frac{1}{1 + j \frac{f}{f_p}} \right) \quad (2-22)$$

where f_p is the cutoff frequency of the low pass filter characterizing the extrinsic limitations. It is crucial for microwave applications that the modulation bandwidth of the VCSEL is sufficiently large so that efficient modulation is achieved as the modulation frequency.

2.3 V-parameter

Lateral-mode control of vertical-cavity surface-emitting lasers (VCSELs) is one of the key issues in realizing high performance optical communication systems, in which single-mode operation is necessary for long and short wavelength regions. High-power single-mode operation is also required for free-space data communication applications. Recently, a two-dimensional photonic crystal (2-D PhC) structure formed on a VCSEL surface has been investigated as a lateral-mode control method. The most attractive feature of this structure is the enlargement of the emission area, thereby permitting higher power output. The large area can be realized because of strong wavelength dependence of the refractive index in the 2-D

photonic crystal structure, analogous to the situation in a photonic crystal fiber. Although good single mode operation has been reported for a specific structure, the optimized design of 2-D photonic crystal structure was not clear, especially when considering a finite etching depth. Since the mode control mechanism utilized in this technology is the effective refractive index control achieved by forming a 2-D photonic crystal structure, a parameter representing this control must have a strong dependence on the etching depth. We have investigated the etching depth dependence, both theoretically and experimentally, of the effective index change in a VCSEL structure.

The 2-D photonic crystal structure with finite etching depth incorporating a single point or a seven-point defect is formed in the top DBR. It is known that the normalized frequency or V-parameter is useful in evaluating the number of guided modes in cylindrical wave guides, an important example being step index optical fibers. The cutoff condition of the first higher mode leads to $V_{eff} = 2.405$, and thus a wave guide with $V_{eff} < 2.405$ is considered to be single mode. In a photonic crystal VCSEL, the effective V-parameter can be expressed by

$$V_{eff} = \frac{2\pi r}{\lambda} \sqrt{n_{eff}^2 - (n_{eff} - \gamma\Delta n)^2} \quad (2-23)$$

where λ is an operating wavelength, r is an equivalent defect radius, n_{eff} is the effective refractive index of the VCSEL cavity [6] without a photonic crystal structure present, D_n is the refractive index reduction introduced by the photonic crystal structure, and g is the hole depth dependence factor that accounts for finite etching depth of the photonic crystal holes in actual photonic crystal VCSELs. The γ factor can be understood qualitatively as proportional to the spatial overlap between the photonic crystal structure and the longitudinal optical power distribution inside the VCSEL structure. Thus, $\gamma = 0$ for vanishing etching depth, $\gamma = 1$ for infinite etching depth, and $\gamma = 0.5$ for holes reaching the middle of the cavity. In the following discussion, the equivalent defect radii of a single point defect and seven-point defect structures are assumed to be $\Lambda-d/2$ and $\sqrt{3}\Lambda-d/2$, respectively, where Λ is a lattice constant and d is the hole diameter of a circular hole of the 2-D photonic crystal

structure. Since we need to investigate larger d/L ratios than those of PCFs,[5] V_{eff} is slightly modified from its appearance in Ref. 5, with the introduction of the V_{eff} - parameter and the modified r in Eq. (2-23). The refractive index variation D_n can be obtained from the photonic band diagram of an out-of-plane propagation mode,[7,8] calculated by assuming that the photonic crystal structure is infinite both in lateral and vertical directions.



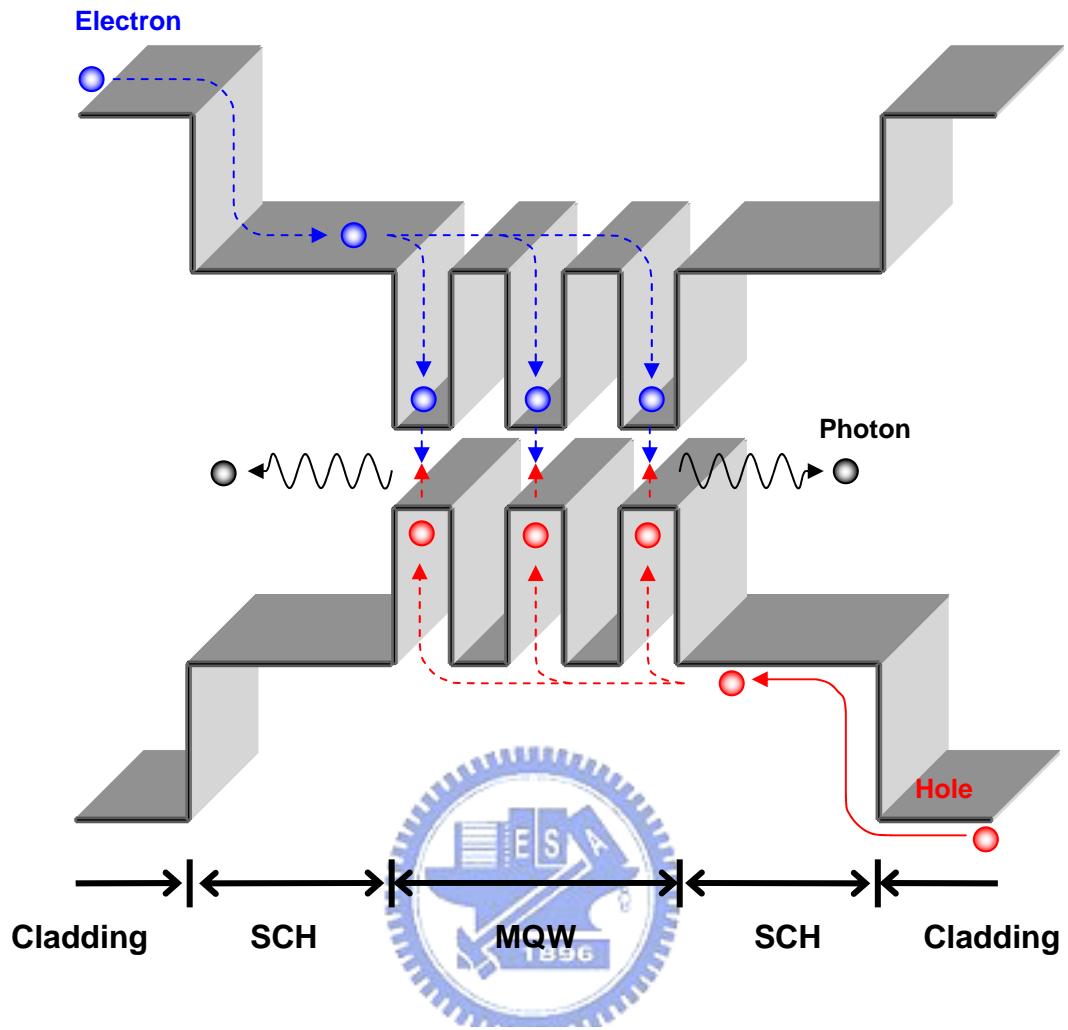
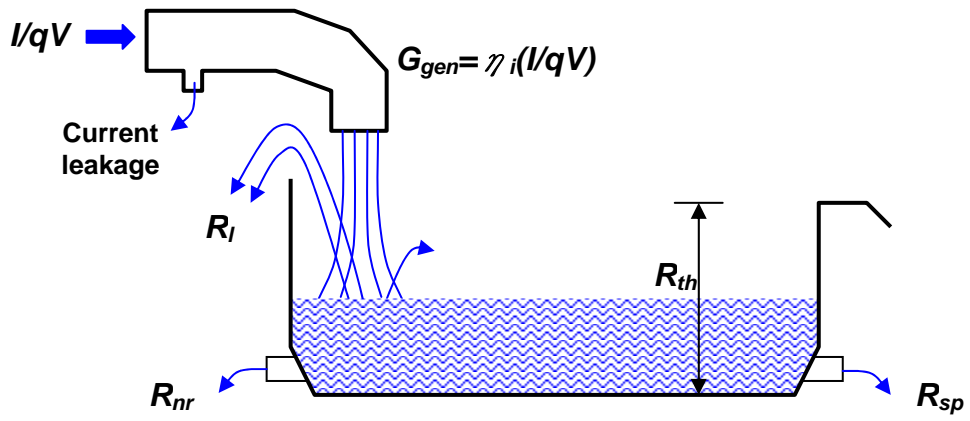
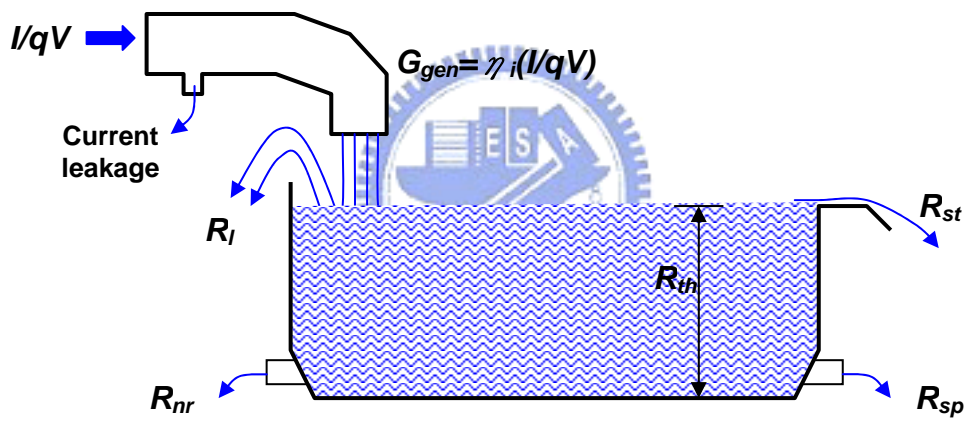


Figure 2-1 Band diagram of active region of VCSEL

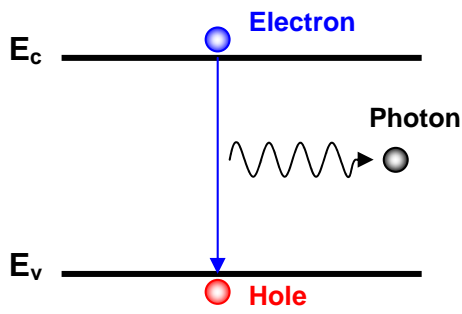


(a)

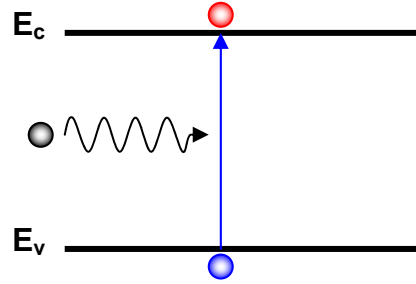


(b)

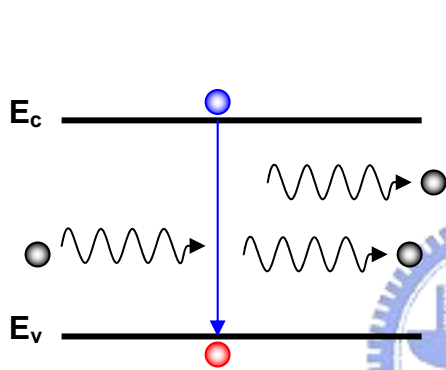
Figure 2-2 Reservoir analogy (a) under threshold (b) above threshold



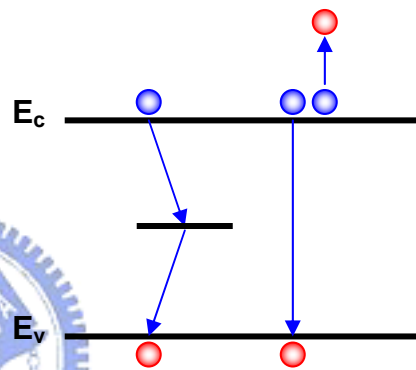
(a) Spontaneous emission



(b) Stimulated generation (absorption)



(c) Stimulated recombination (emission)



(d) Nonradiative recombination

Figure 2-3 Basic electronic recombination/generation mechanism

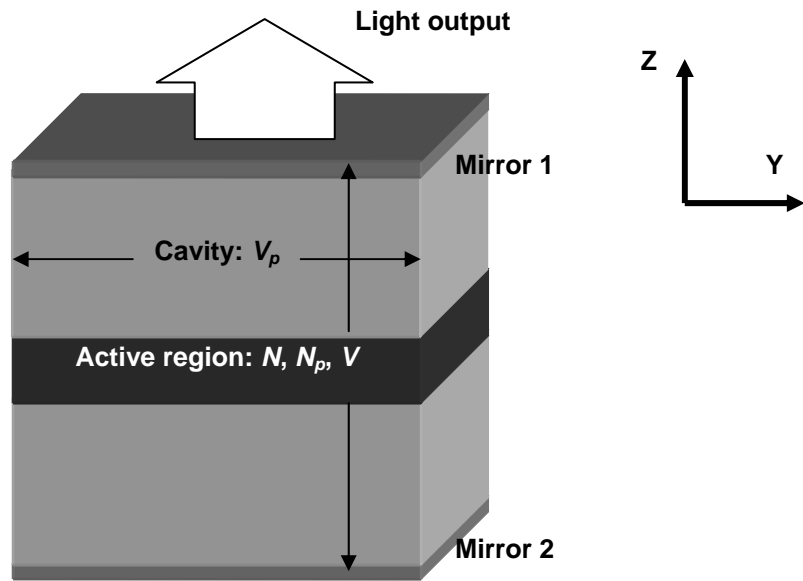


Figure 2-4 Schematic of VCSEL illustrating active region and cavity volumes

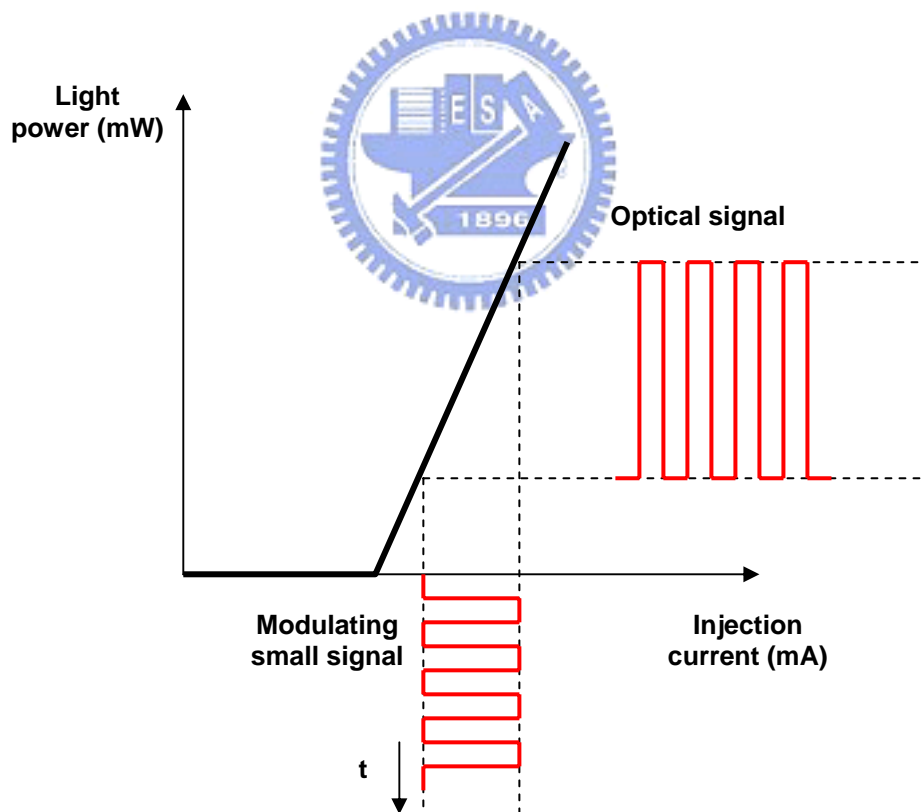


Figure 2-5 Conversion from electrical small signal train into optical signal

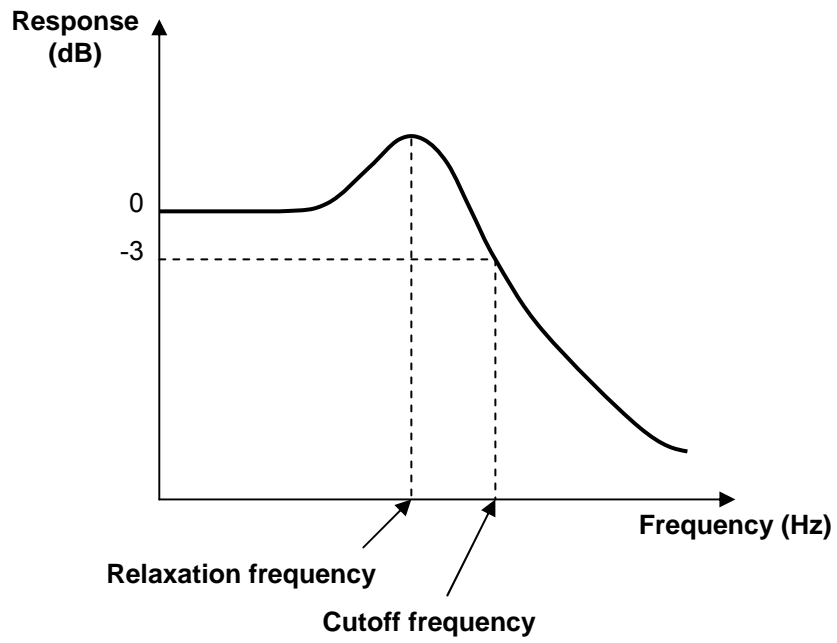


Figure 2-6 Small signal modulation response of a VCSEL



Chapter 3

VCSEL fabrication and measurement setup

In this chapter, we presented the fabrication method of VCSEL, instrument setup for electrical and optical characteristics measurement. The fabrication techniques for VCSEL such as air-post, regrowth, proton-implantation, selective oxidation and reactive ion etch (RIE) had been employed to define the current path, gain region, carrier and the optical confinement. With in these techniques, the VCSEL fabricated by proton-implantation and reactive ion etch (RIE) had some superior properties such as simple and stable process. The design principles of VCSEL wafer structure were based on the method described as follow section. Finally, probe station system, spectrum measurement system , the establishments of eye diagram measurement system and far field pattern measurement system were described as follows.

3.1 Fabrication of tapered and blunt oxide VCSEL

A vertical cavity surface emitting laser consisted of multi-quantum-well sandwiched between two highly reflective distributed Bragg reflectors (DBRs). The 850nm GaAs / AlGaAs VCSEL devices studied here were grown by MOCVD on the Si-doped GaAs substrate. The bottom DBR had 39.5 pairs of alternating $\text{Al}_{0.15}\text{Ga}_{0.85}\text{As}$ / $\text{Al}_{0.9}\text{Ga}_{0.1}\text{As}$ pairs with quarter-wavelength-thick layer. The active region was consisted of three GaAs / AlGaAs quantum wells and cladding layer. The top DBR had 22 pairs of alternating $\text{Al}_{0.15}\text{Ga}_{0.85}\text{As}$ / $\text{Al}_{0.9}\text{Ga}_{0.1}\text{As}$ layer. A high Al-content selective oxidation layer, $\text{Al}_{0.98}\text{Ga}_{0.02}\text{As}$, was inserted just three layers above the active region. The VCSEL structure was trenched a ring of mesa, indicated in [Figure 3-1](#), in order to execute oxidation process, which still improved current spreading effect. A bridge connected with contact ring and bond pad for current injection. Mesa structure benefited reducing current path and inducing optical confinement. Passivation layer coating, used of SiN_x , formed an isolation layer reducing leakage current below metal contact. The detailed process of oxide-implant VCSEL was desired as [Figure 3-2](#).

The scheme of oxidation process system was drawn in [Figure 3-3](#). The VCSEL

was placed into center of furnace and purge by N_2 . The furnace annealed approach $420^\circ C$ then imported the invariable flow-rate of steam into furnace for fixed time. Oxidation time was crucial for the process for forming different oxide apertures. The oxide-extent was almost linear relative to oxidation time, shown in [Figure 3-4](#). For blunt oxide VCSELs, a 30-nm-thick $Al_{0.98}Ga_{0.02}As$ layer was placed in node position. For tapered oxide VCSEL, the tapered oxide layer was formed of a 10-nm-thick $Al_{0.99}Ga_{0.01}$ layer adjacent to a 200-nm-thick $Al_{0.98}Ga_{0.02}As$ layer, which is similar to Ref. [9]. Multiple proton implantations with a dose in the range of $10^{13} \sim 10^{15} \text{ cm}^{-2}$ and four different proton energy ranges between 200 to 420 keV were adapted according to simulation results of the stopping and range of ions in matter (SRIM). The implantation region was kept away from the mesa to prevent damage to the active region and consequent voiding of triggering reliability issues. A series VCSELs with different type of oxide layer were fabricated in the same implant process condition and their static and dynamic characteristics in were presented in chapter 4.

3.2 Fabrication of photonic crystal VCSEL

3.2.1 Fabrication of oxide photonic crystal VCSEL



The epitaxial layers of the PC-VCSEL's wafer structure were grown on the n^+ -GaAs substrate by metal-organic chemical vapor deposition (MOCVD). The bottom distributed Bragg reflector (DBR) consists of a 30.5-pair n-type (Si-doped) quarter-wave stack of $Al_{0.12}Ga_{0.88}As/AlAs$. The top DBR consists of 22-period p-doped (carbon-doped) $Al_{0.12}Ga_{0.88}As/AlAs$ quarter-wave stack. Above that is a heavily doped p-type GaAs contact layer. The graded-index separate-confinement heterostructure (GRINSCH) GaAs/AlGaAs active region has an undoped three-quantum-well (3QWs) GaAs/ $Al_{0.3}Ga_{0.7}As$, a lower linearly-graded undoped $Al_xGa_{1-x}As$ ($x = 0.6 \rightarrow 0.3$) waveguide layer and an upper linearly-graded undoped $Al_xGa_{1-x}As$ ($x = 0.3 \rightarrow 0.6$) waveguide layer. The process was similar to oxide-confined VCSEL. After that, hexagonal lattice patterns of photonic crystal with a single-point defect were defined within the p-contact ring using photolithography and etched through the p-type DBR by using a reactive ion etch (RIE). The lateral index around a single defect can be controlled by the hole diameter (a) to lattice constant (Λ) ratio

and etching depth [10]. This ratio (a/Λ) is 0.5; the lattice constant Λ is 5 nm in the PC-VCSEL and the etching depth of the holes is about 17 pairs out of 22 pairs of the top DBR layers. The device structure, top view image of the PC-VCSEL, and the scanning electron microscope image of an etched hole were shown in Figure 3-5. And the detailed process of oxide photonic crystal VCSEL was desired as Figure 3-6.

A series oxide photonic crystal VCSELs with different (a/Λ) ratio were fabricated in the same implant process condition and their static characteristics in were presented in chapter 4.

3.2.2 Fabrication of implant photonic crystal VCSEL

The process was similar to oxide photonic crystal VCSEL. The proton (H^+)-implanted VCSEL was fabricated before combination with photonic crystal holes. First, the p-contact ring with an inner diameter of 24 to 46 nm was deposited on the top of the p-contact layer and an n-contact was deposited on the bottom of an n^+ -GaAs substrate. The device was annealed at 430 °C under N_2 ambient. The current confinement of the device, with a diameter of 10 nm, was then defined by proton implantation. The implantation energy was 270 keV, with a dosage of 6×10^{14} cm^{-2} . After that, the follow-up process was the same with the oxide photonic crystal VCSEL. The device structure is shown in Figure 3-7.

A series implant photonic crystal VCSELs with different (a/Λ) ratio were fabricated in the same implant process condition and their static characteristics in were also presented in chapter 4.

3.3 Probe station and spectrum measurement system

Probe station system was essential instrument for basic characteristics measurement such as I-L (current versus light output), I-V (current versus voltage). Scheme of probe station system, illustrated in Figure 3-8, contained probe station, current source, and power-meter module. Keithley 238 as current source supplies continuous current for diode laser and receives relative voltage synchronously. Laser output power is measured by Newport power-meter module (model 1835C). With these data, we could plot the trend of L-I-V associated with computer. For accuracy

power measurement, an integration sphere was used to pick up whole light output from VCSEL.

For basic measurement, VCSEL device was placed on platform of probe station and injected bias current with microprobe. We could observe threshold condition, slope efficiency, turn-on voltage and differential resistance as L-I-V information by sweeping bias current injection. Distribution of transverse mode power is metered as near-field pattern. Near-field pattern (NFP) is still obtained by specific CCD and traces out results with computer. Beam-view analyzer is useful software we used in taking NFP. We could obtain NFP image under threshold, as spontaneous emission, to define oxide aperture size.

Emission spectrum was measured by Advantec optical spectrum analyzer (OSA). We served a multi-mode fiber bundle on probe close to emission aperture in focus for taking spectra. OSA had small spectrum resolution as 0.1nm for accurately measuring VCSEL lasing spectrum. Scheme of spectrum measurement system was combined with probe station as [Figure 3-8](#).

3.4 Far field pattern measurement system

Distribution of divergence angle is metered as far -field pattern. We used a long work distance objective (20X,Nikon), fixed in a triple-divide translation stage, to pick up the laser output from VCSEL. Light was received by CCD(coherent 4800) . Far-field pattern (FFP) is still obtained by specific CCD and traces out results with computer. Beam-view analyzer is useful software we used in taking FFP. We could obtain FFP image under threshold, to define divergence angle illustrated with [Figure 3-9](#).

3.5 Microwave test and eye diagram measurement system

The experimental setup for measuring eye diagrams is illustrated in [Figure 3-10](#). The VCSELs were probed using a high-frequency coplanar microwave probe (Picoprobe Model 40A) had 700 μ m pitch (ground (G) to signal (S) tip spacing) and

suitable frequency range was up to 40 GHz. Signal probe was higher than ground tips. Fine probing was observed by signal probe skating on contact substrate. Laser diode drivers (Newport, model 525) provided direct current signal to set the laser above the threshold. Bias-Tee combined AC and DC signal transmission through the same coaxial cable. A bias current was combined with a pseudorandom bit sequence of $2^{31}-1$ from a 12.5-Gb/s pattern generator (Anritsu MP1764C). Optical platform contained microscope, beam splitter, objective and fiber coupler etc.. We used a long work distance objective (20X, Mitutoyo), fixed in a triple-divide translation stage, to pick up the laser output from VCSEL. Light was separated by beam splitter and received by CCD and another 10X objective (Olympus). One of splitting light was received by a simplified microscope, which was constructed by beam splitter and CCD to make probing easily. Another light path through 10X objective coupling into multimode fiber by five-axis fiber aligner (Newport). The laser output was focused using two object lenses into a 62.5 micrometre-diameter graded index multimode fiber and transmitted a short distance to a 12-GHz photoreceiver (New Focus 1580-LF). The lenses serve to capture all the different modes despite their different divergence. The electrical signal was amplified by the receiver before entering the 12.5-GHz digital oscilloscope (Agilent 86100A), triggered by the pattern generator.

3.6 Experimental guidelines

Special attention must be paid to the modulation depth of the signal applied to the lasers. High modulation amplitude increases the signal to noise ratio but can introduce distortions of the response due to nonlinearities and cause an artificial compression of the resonance frequency peak, especially with structures operating at very low bias currents such as oxidized VCSEL with sub-milliampere threshold.

For accurate parameter extraction it is also important to have a large signal-to-noise ratio. This can be achieved by using large temporal averaging factors during measurements. Averaging in the frequency domain, so-called smoothing is not recommended; it will reduce the frequency resolution of the signal and often corrupt the phase information.

A good rule is to measure the modulation response at 5 – 10 bias current until a maximum current is reached where the resonance frequency peak saturates or starts to decrease.

At high frequency the signal to noise ratio is often poor. This noise in the high frequency region is in general not only caused by ordinary amplifier noise but also noise due to calibration problems of the measurement set-up. Even slight movement of the measurement cables will change the phase of distant reflections, which can give a noisy appearance of the measurement curve. Crosstalk can give similar effects. This type of noise is not uncorrelated at different measurement points and is difficult to distinguish from the signal. Hence, it is preferable to omit the highest frequency parts of the measurements where the signal where the signal-to-noise ratio is very poor.

The VCSEL chip has to be mounted on a module for commercial applications. The package has limitations at high frequencies and the measured bandwidth can be strongly decreased by the package parasitics. Resonance and filtering effects introduced by the inherent package parasitics can be significant sources of error. The inductive and capacitive elements associated with the physical geometry of the package will result in small parasitic LC circuits, which will in turn cause voltage or current peaking at the resonance frequencies and low pass or band rejection filtering effect at other frequencies.



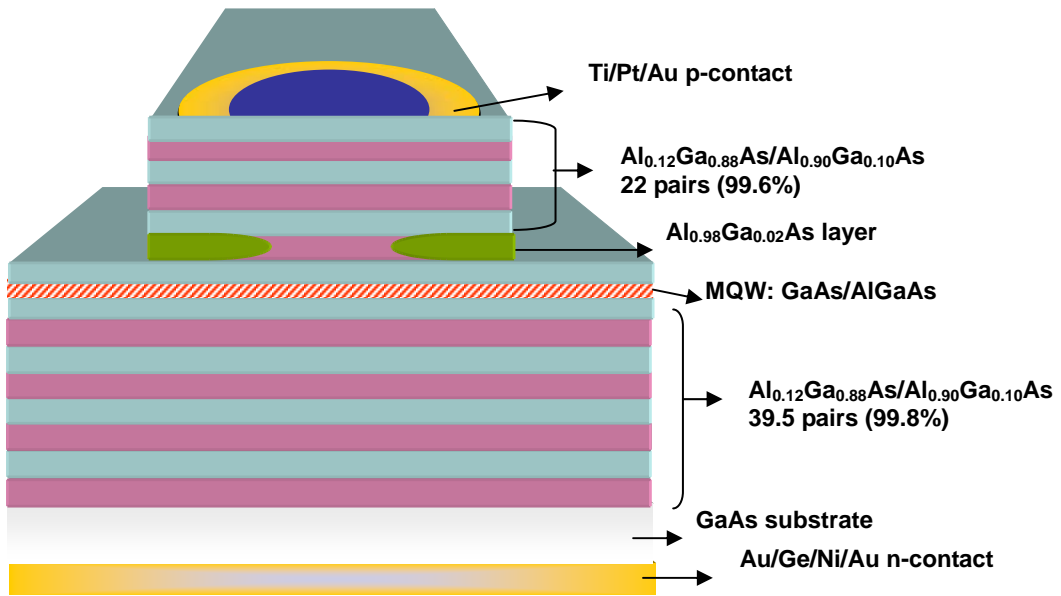


Figure 3-1 Cross section structure of tapered oxide implant VCSEL structure



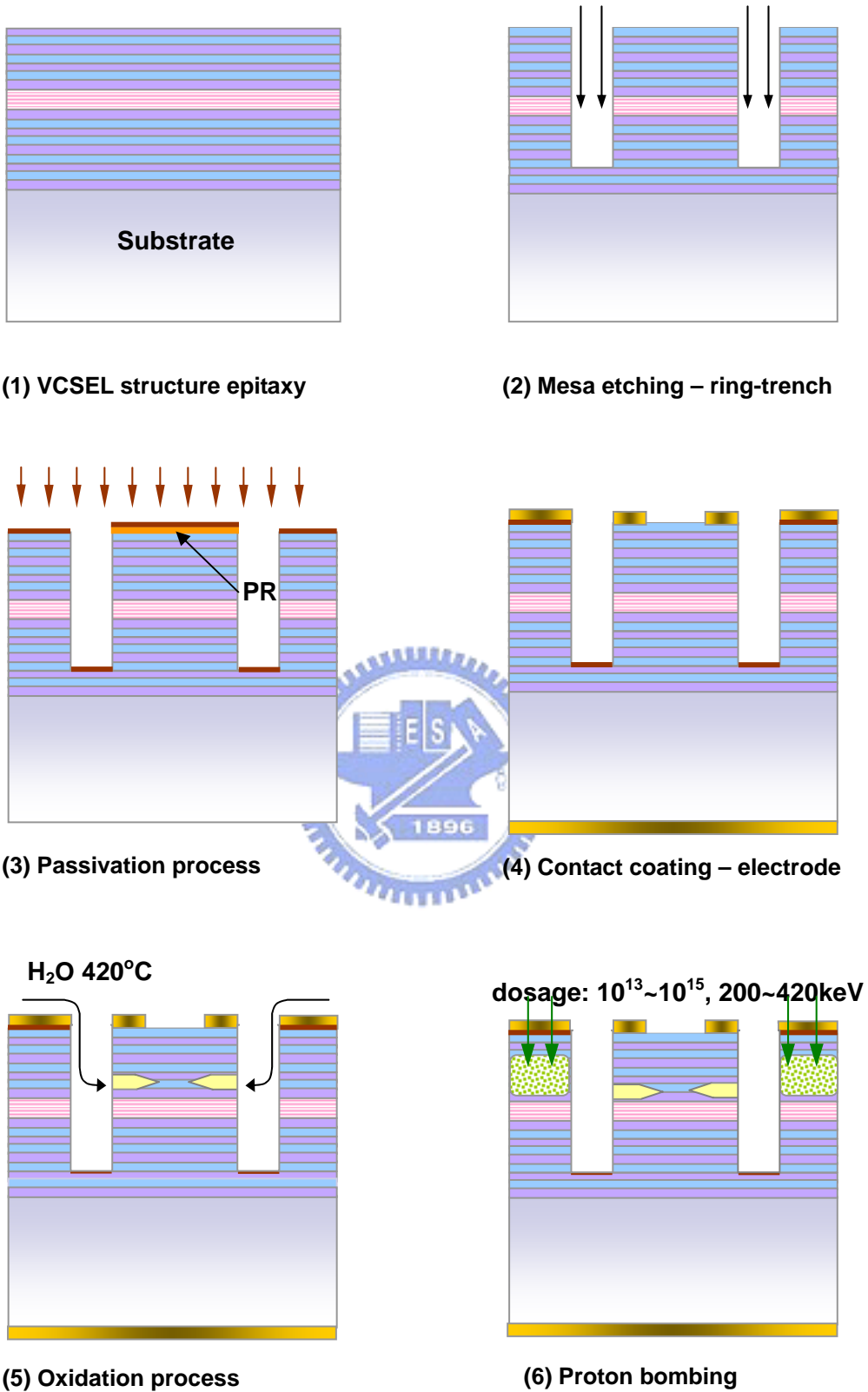


Figure 3-2 Steps of oxide-implant VCSEL process

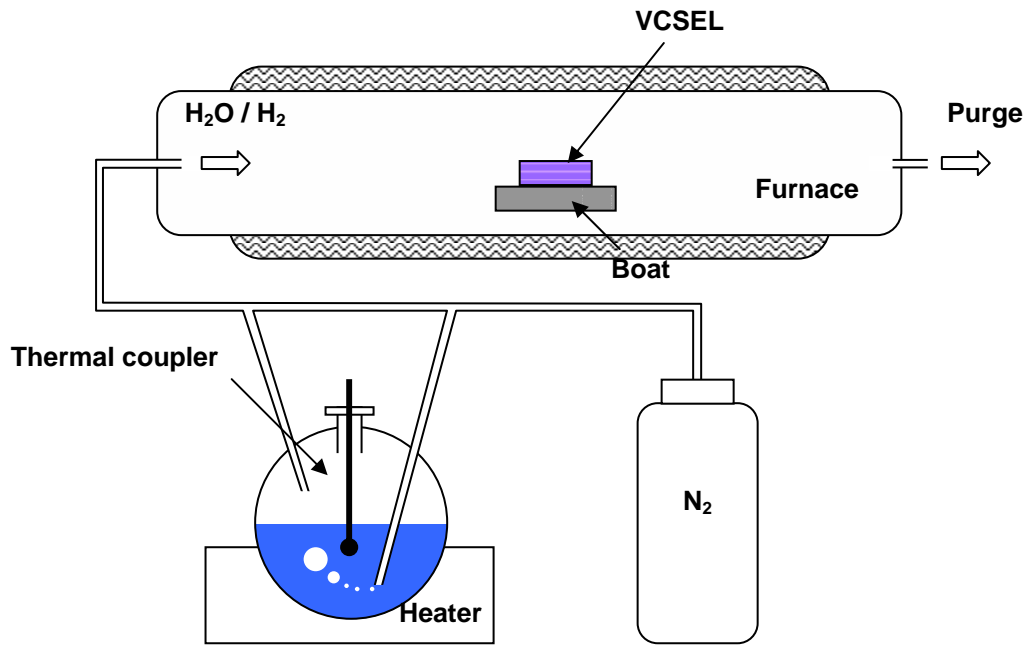


Figure 3-3 Illustration of oxidation process system setup

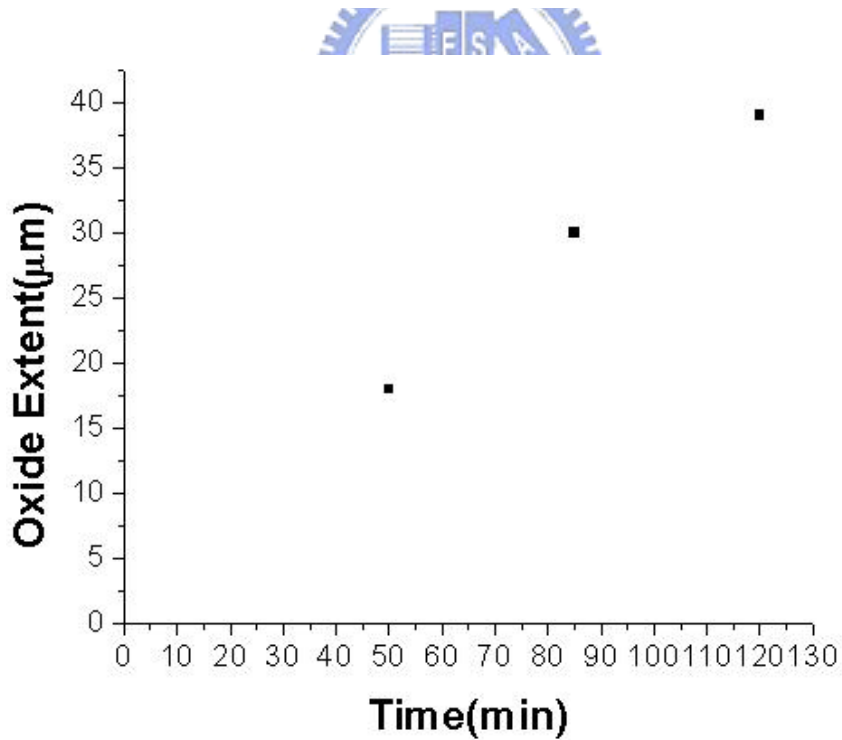
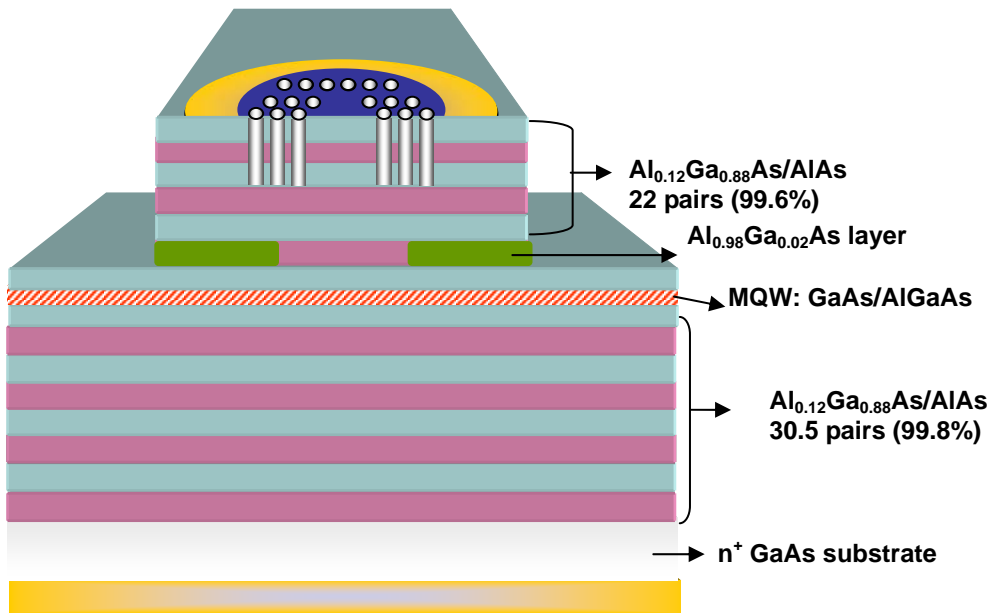
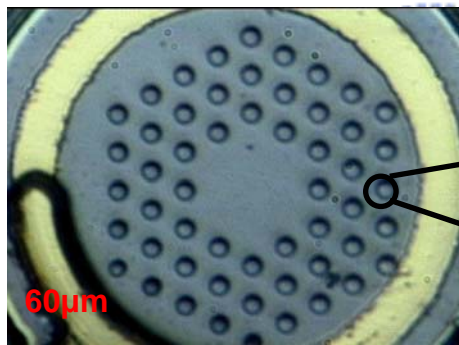


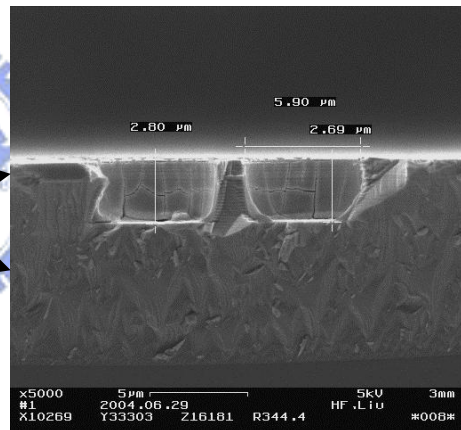
Figure 3-4 Oxidation rate of 98% Al-content layer



(a)

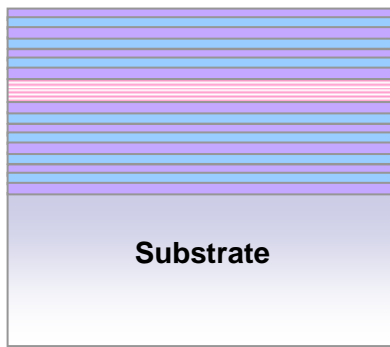


(b)

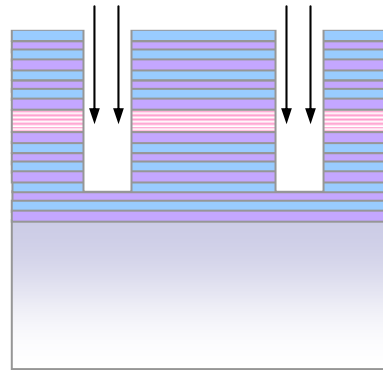


(c)

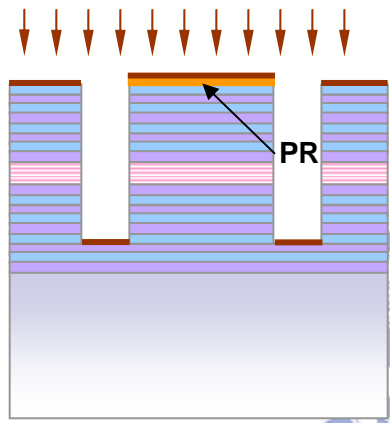
Figure 3-5 (a) Cross section structure of oxide photonic crystal VCSEL structure (b) top view image of the PC-VCSEL;(c) scanning electron microscope image of an etched hole.



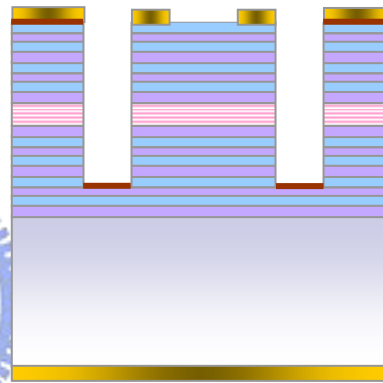
(1) VCSEL structure epitaxy



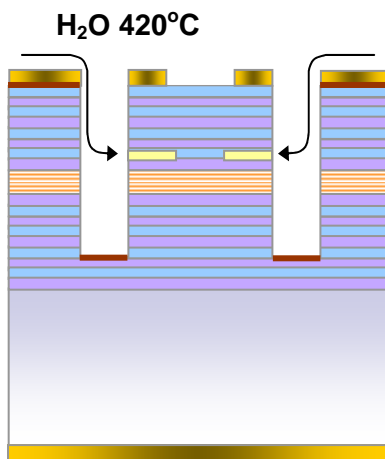
(2) Mesa etching – ring-trench



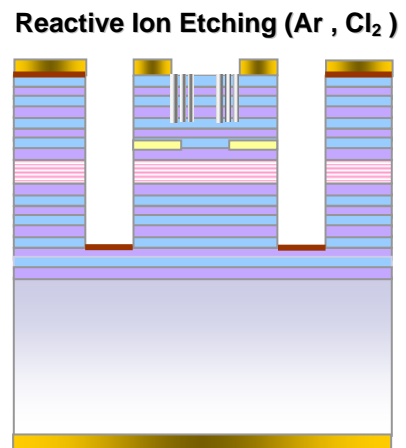
(3) Passivation process



(4) Contact coating – electrode



(5) Oxidation process



(6) Etching air hole

Figure 3-6 Steps of oxide photonic crystal VCSEL process

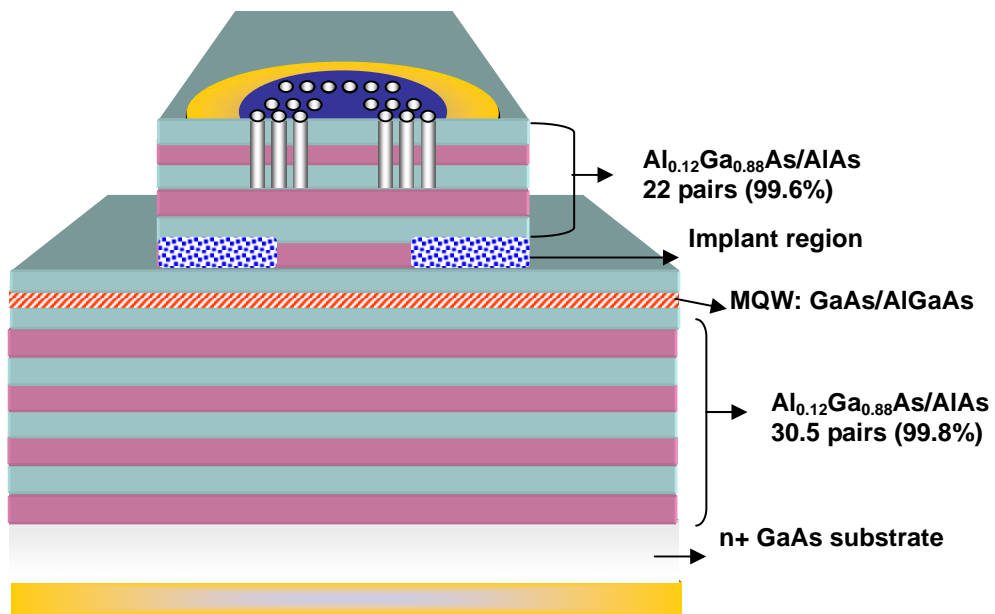


Figure 3-7 Cross section structure of implant photonic crystal VCSEL



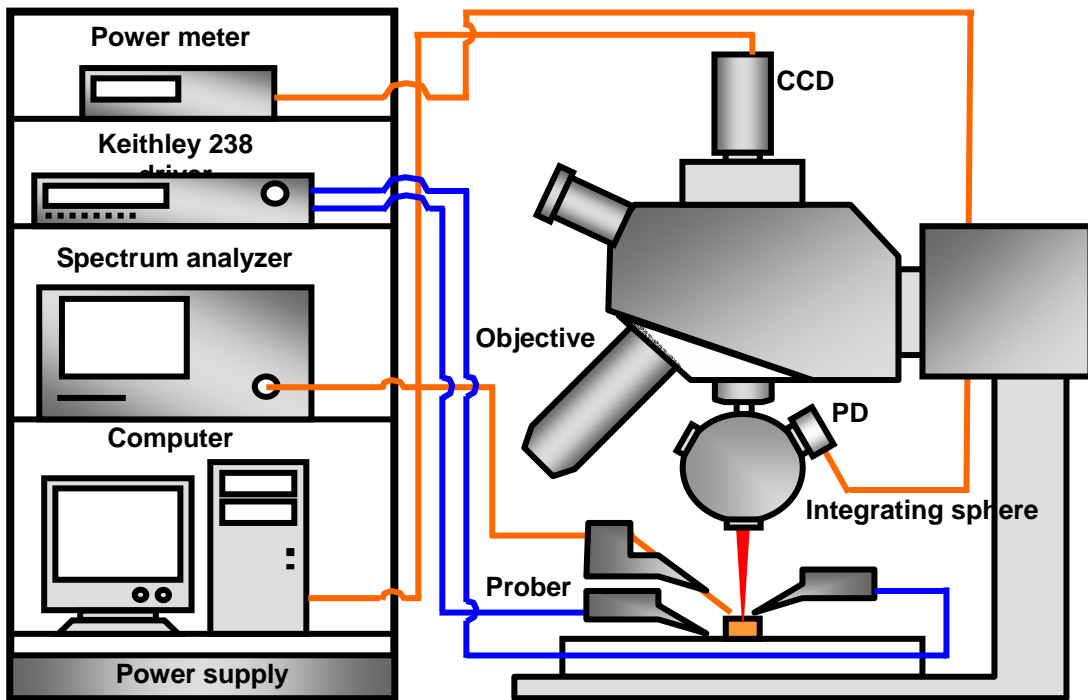


Figure 3-8 Probe station measurement instrument setup

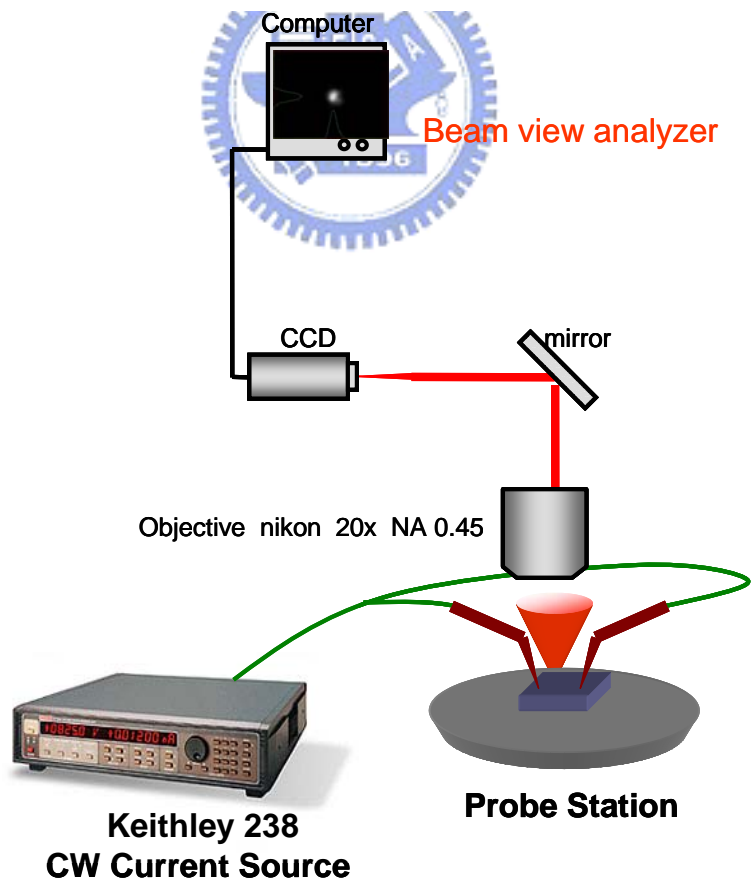


Figure 3-9 Far field pattern measurement system

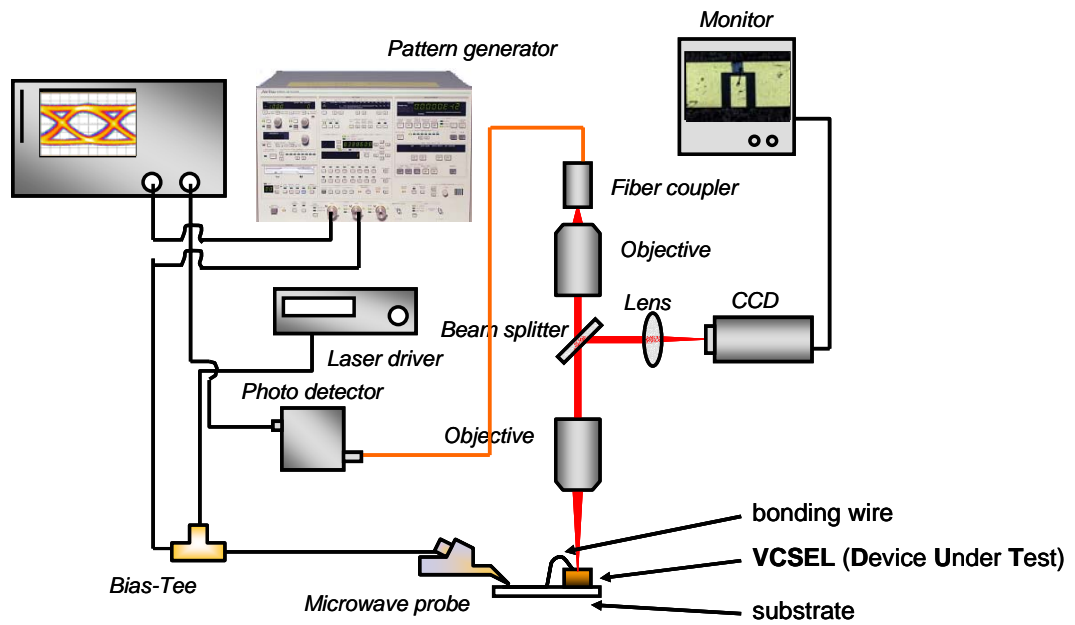


Figure 3-10 eye diagram measurement instrument setup



Chapter 4

Result and discussion

Oxidation process was regular process for VCSEL fabrication. Most high speed VCSEL was also made by the same method. In our study, we chose different type of oxide implant VCSELS to compare with their high speed characteristics in first section. In second section, we was according to the static and high speed characteristics of these VCSELS to modeling the equivalent circuit. Equivalent circuit modeling was investigated in section 4-2. With VCSEL modeling, the equivalent components were extracted and observe the modulation limitation caused by structure. In third section, we chose different type of photonic crystal VCSELS to compare with their static characteristics of these VCSELS

4.1 Oxide-implant VCSELS DC and AC characteristics

Tapered oxide VCSEL and blunt oxide VCSEL had same process structure, shown in [Figure 4-1](#). Process structure was described in Chapter 3. Both VCSEL had the same oxide aperture as 5.5 μm and mesa as 30 μm .

The static characteristics of both VCSEL were shown in [Figure 4-2](#). The threshold current is ~ 1 mA (0.9 mA) for tapered (blunt) type VCSELS with the same slope efficiency of ~ 0.35 mW/mA. The similar static performance is not surprising since 1. the oxide apertures here have the same size of 5~6 μm and 2. the blunt oxide don't incur excess scattering except at very small oxide size ($< 3\mu\text{m}$). The maximal output power exceeds 3 mW at room temperature and output power rollover occurs as the current increases above 12 mA.

The measured modulation response curves for tapered oxide VCSEL and blunt oxide VCSEL were shown in [Figure 4-3\(a\)](#) and [4-3\(b\)](#), respectively. The maximum modulation bandwidth of both VCSEL was 13 and 9.5 GHz. At low bias currents, the bandwidth increased in proportion to the square root of the current above threshold, as expected from the rate equation analysis. For blunt oxide VCSEL, low frequency rollover was observed and the modulation response became gradually overdamped

as the bias current increasing. In contrast, no rollover was observed in low frequency for tapered oxide VCSELs and the 3-dB bandwidth reached a maximum value of 13 GHz before fully overdamped. The observations coincide with the simulation results for blunt oxide VCSEL in which a significant overdamping was reported in the relaxation oscillation due to the nonuniformity of the transverse mode and significantly reduced the modulation bandwidth. [11, 12] The bandwidth are similar at low bias current for both tapered oxide VCSELs and blunt oxide VCSELs and saturated at the bias current higher than 8 mA. Modulation current efficiency factor (MCEF), indicated in Figure 4-4, appeared modulation bandwidth as function of $(I-I_{th})^{1/2}$. Tapered oxide VCSEL had $6.5 \text{ GHz}/\text{mA}^{1/2}$; As the Figure 4-5 shows, the peak height of modulation response was higher in the tapered oxide VCSEL than that of blunt oxide VCSEL. The higher modulation amplitude in tapered oxide VCSELs implies the lower damping rate which was known to approximately proportion to the ratio between resonant frequency and peak modulation amplitude [13]. The oxide layer of tapered oxide VCSEL had was theoretically investigated to reduce the nonlinear damping effect by making the electrical aperture smaller than the optical aperture, and thereby improves the modulation bandwidth [12].

As the Figure 4-3 shows, the peak height of modulation response was higher in the tapered oxide VCSEL than that of blunt oxide VCSEL. The higher modulation amplitude in tapered oxide VCSELs implies the lower damping rate which was known to approximately proportion to the ratio between resonant frequency and peak modulation amplitude [13]. In depth, the damping rate, resonant frequency, and parasitic roll-off frequency can be obtained by fitting the experimental data to a three-pole approximation of the modulation response equation [13]. The K factor can be found out from the slope of damping rate with the square of resonant frequency, as plotted in Figure 4-5. It was shown the damping rate indeed about two times higher than that in blunt oxide VCSELs and the K factors were 0.15 ns and 0.4 ns respectively. The comparison of the damping rate is also coincident with the theoretical prediction [11, 12]. If parasitic and other heating effects are ignored, the theoretical damping limited 3-dB bandwidth may be over 59 GHz for tapered oxide VCSEL and 22 GHz for blunt oxide VCSEL, from the ration of $2\pi(2)^{1/2}/K$. [13]

For commercial high speed performance testing, tapered oxide and blunt oxide VCSEL were measured as eye diagram shown in Figure 4-7. Eye diagram of blunt

oxide VCSEL shown that jitter was about 25 ps. Tapered VCSEL had small jitter below 20 ps. It still had rise-time/fall-time were 26 and 40 ps respectively. For that, oxide-implant VCSEL passed 10Gbps clarified.

4.2 Equivalent circuit modeling

As previously shown in [Figure 4-3\(a\)](#), the 3-dB bandwidth reached a maximum value of ~ 13 GHz before fully overdamped. We therefore investigate the extrinsic bandwidth limitation on the tapered oxide VCSELS in the next. An equivalent circuit for the VCSEL impedance is useful for analysis of electrical bandwidth limitations. Inset of [Figure 4-6](#) shows the equivalent circuit model used to extract the circuit components. The resistance R_m represents the mirror loss while the R_a accounts for active region resistance. C_a represents a combination of capacitance of active area and oxide layer. A shunt resistance R_p is also included to account for pad loss and the pad capacitance is represented by C_p . Using this equivalent circuit, we can also investigate the extrinsic limitations on the modulation speed and determine the influence of the parasitic capacitance and the mirror resistance on the modulation bandwidth. To extract the capacitance of VCSELS, the measured amplitude and the phase of S_{11} data were fitted from 100 MHz to 20 GHz. Fig. 5 illustrates measured and fitted S_{11} results of the tapered oxide VCSEL at 6mA. Convergence of the fitting values to physically reasonable values was obtained using the following procedure. First, the C_p , R_p , R_m , C_a were extracted using zero bias S_{11} data (where R_a is very large and can be neglected). Second, the R_a and C_a values were extracted by fitting the S_{11} data for different bias currents. Finally, all the circuit parameters were allowed to vary about these values in order to minimize the squared error. The resulting C_p , R_p , and R_m were 160 fF, 5Ω and 51Ω respectively and the extracted R_a and C_a values for different bias currents were listed in [Table 4-1](#). Based on these extracted values, the electrical bandwidth can be determined from -3dB of the S_{21} of the equivalent circuit shown in inset of [Figure 4-6](#). In consequence, electrical bandwidth of ~ 12.5 GHz was obtained and showed weak dependence on bias current. The calculated electrical bandwidth is coincident with the maximal measured modulation bandwidth and confirms the parasitic effects as the main limitation on the tapered oxide VCSELS.

4.3 Photonic crystal VCSELs DC characteristics

Oxide VCSEL and oxide photonic crystal VCSEL had same process structure, shown in [Figure 4-8](#). Process structure was described in Chapter 3. Both VCSEL had the same oxide aperture as 12 μm and mesa as 50 μm .

The static characteristics of both VCSEL were shown in [Figure 4-9](#). The threshold current is ~ 0.9 mA (0.5 mA) for oxide (photonic crystal) type VCSELs. The slope efficiency of oxide (photonic crystal) VCSELs ~ 0.239 mW/mA (0.254 mW/mA). The series resistance of oxide (oxide photonic crystal) VCSELs $\sim 145 \Omega$ (191 Ω). The maximal output power exceeds 2.8(1.61) mW at room temperature.

The photonic crystal VCSEL with $\Lambda=5$ nm, $a/\Lambda=0.4$ exhibits single fundamental mode lasing on the low current range of operation with the side-mode suppression ratio (SMSR) of over 20 dB as shown in [Figure 4-10 \(a\)](#). But as a result of the oxide layer was influence on the index guide of photonic crystal. Therefore the photonic crystal VCSEL becomes multi-mode lasing over the high current range of operation as shown in [Figure 4-10 \(b\)](#). The near field images of the device also shown in the inset of [Figure 4-10](#). Very strong emission can be seen in the central site, where the circular emission pattern is evidence of the PC confined mode as shown in [Figure 4-10 \(a\)](#).

The process structure Implant photonic crystal VCSEL as shown in [Figure 4-11](#). Process structure was described in Chapter 3. The oxide aperture of Implant photonic crystal VCSEL as 10 μm and mesa as 60 μm

The static characteristics of implant photonic crystal VCSEL were shown in [Figure 4-12](#). The threshold current is ~ 1.25 mA for implant photonic crystal VCSELs. The slope efficiency of implant photonic crystal VCSELs ~ 0.18 W/A. The series resistance of implant photonic crystal VCSELs $\sim 1.5\text{K} \Omega$. The maximal output power exceeds 1.24 mW at room temperature.

Lasing spectra of the implant photonic crystal VCSEL is shown in [Figure 4-13\(a\)](#), confirming singlemode operation within overall operation current. The PC-VCSEL reveals a side mode suppression ratio(SMSR) > 40 dB throughout the current range. For comparison, lasing spectra of a proton-implanted VCSEL without photonic crystal holes shows multiple mode operation as the driving current increased above 4.25 mA [Figure 4-13\(b\)](#). As the driving current increases, even higher-order transverse modes emerge.

We present the far-field intensity distribution of implant VCSEL in [Figure 4-14\(a\)~\(c\)](#). The far-field image shows a doughnut-like pattern at injection current of 3.8mA (i.e. $1.1 I_{th}$), which is illustrated in [Figure 4-14\(a\)](#). At higher injection current of 4.9 mA(i.e. $1.3 I_{th}$), some radial structures appear at the periphery of doughnut-like pattern, which is illustrated in [Figure 4-14\(b\)~\(c\)](#). It can be seen that multiple transverse modes could be observed when the drive current equals 3.8mA (i.e. $1.1 I_{th}$). On the other hand, the intensity of higher order mode and the beam divergence angle both increase as the drive current is increased to 4.9 mA(i.e. $1.3 I_{th}$).

The far-field intensity distribution of implant photonic crystal VCSEL in [Figure 4-14\(d\)~\(f\)](#). The far-field image shows a doughnut-like pattern at injection current of 2.8mA (i.e. $1.1 I_{th}$), which is illustrated in [Figure 4-14\(a\)](#). At higher injection current of 3.5 mA(i.e. $1.3 I_{th}$), some radial structures appear at the periphery of doughnut-like pattern, which is illustrated in [Figure 4-14\(b\)~\(c\)](#). It can be seen that only fundamental modes could be observed when the drive current equals 2.8mA (i.e. $1.1 I_{th}$). On the other hand, the beam divergence angle increases very small as the drive current is increased to 3.5 mA(i.e. $1.3 I_{th}$). [Figure 4-15](#) shows beam divergence angles as functions of VCSELs drive current. It was found that by incorporate with photonic crystal, the divergence angle was decrease. And the divergence angles of single mode VCSEL was not increase with current.

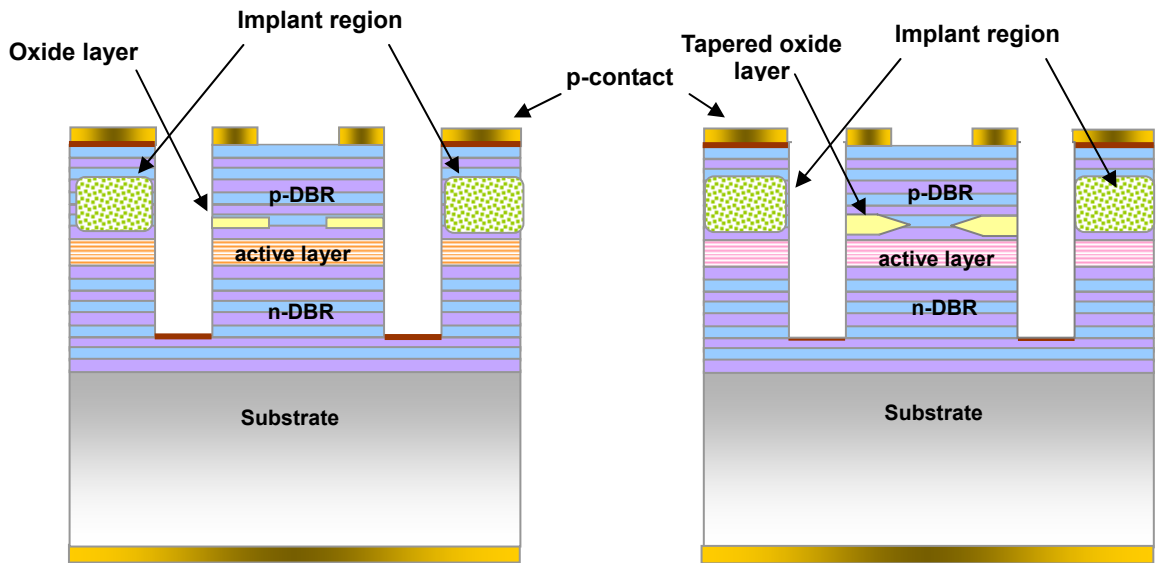


Figure 4-1 Tapered oxide and blunt oxide VCSEL structure

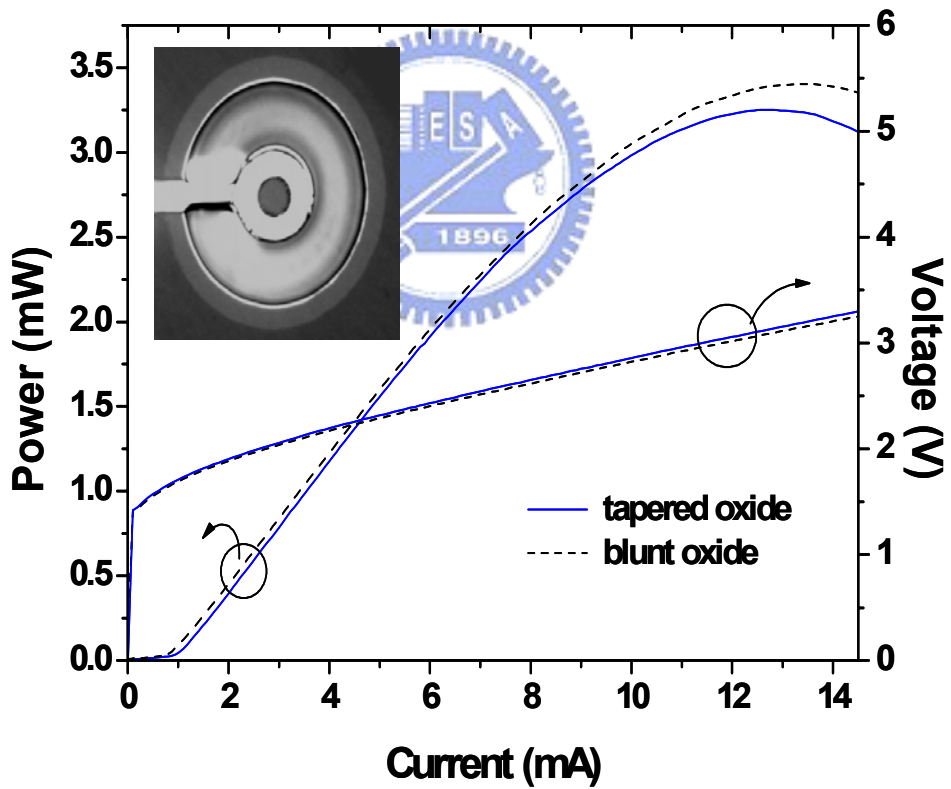
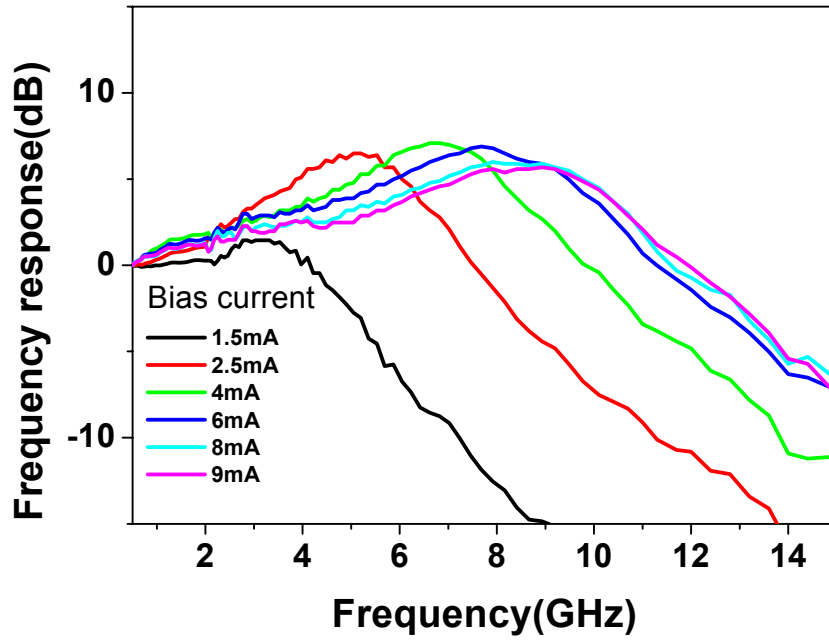


Figure 4-2 Typical LIV curve for tapered oxide and blunt oxide VCSELs



(a) Tapered oxide VCSEL

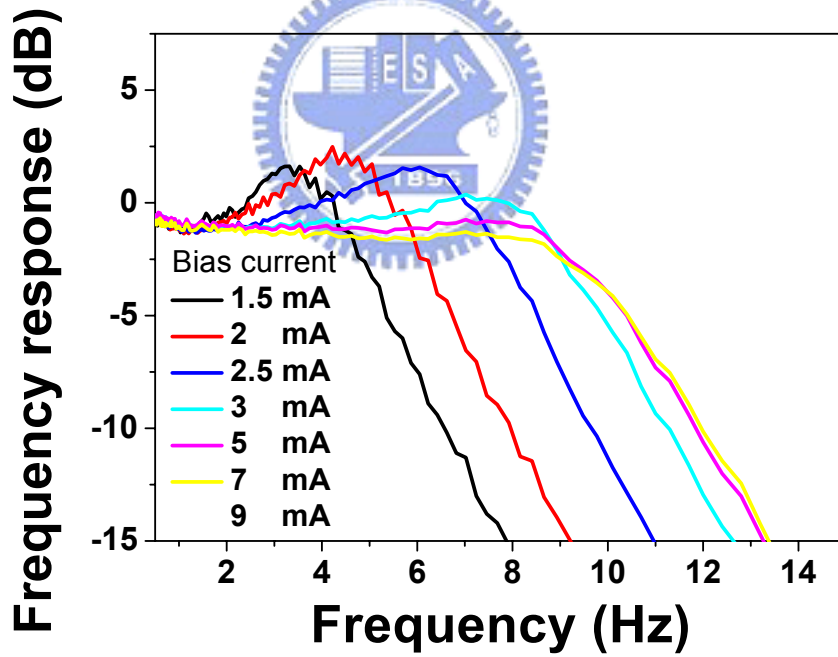


Figure 4-3 Modulation responses for both tapered oxide and Blunt oxide VCSELs

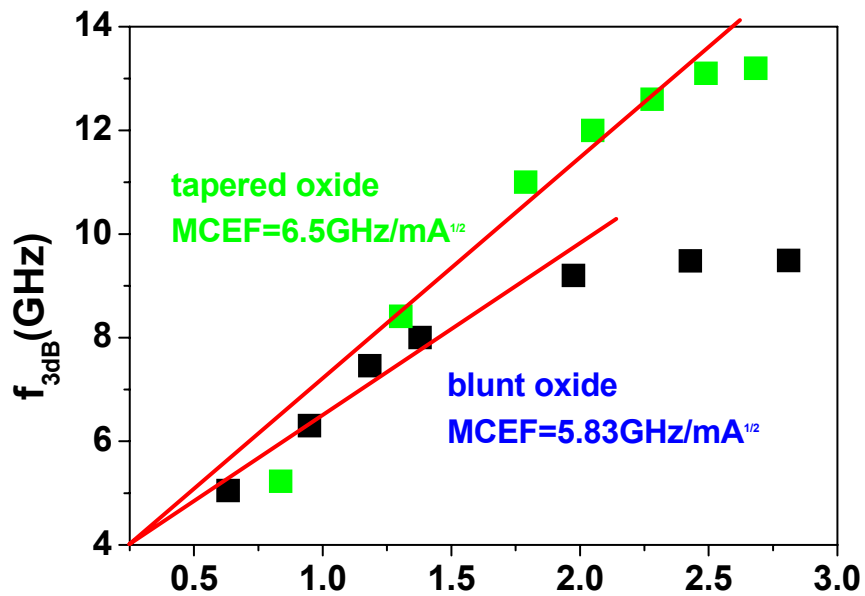


Figure 4-4 3dB frequency as a function of $(I-I_{th})^{1/2}$ for tapered oxide and blunt oxide VCSELs

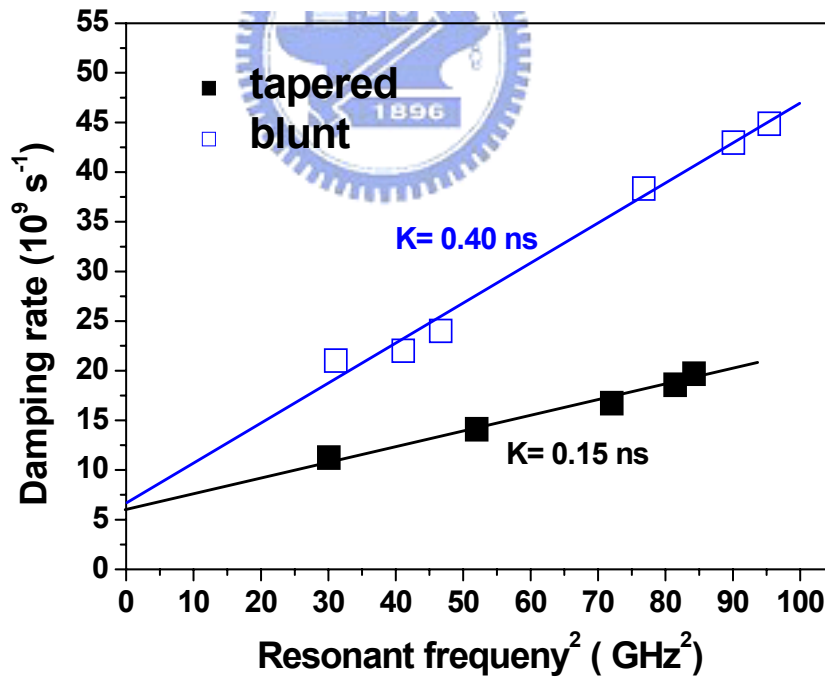


Figure 4-5 damping rate as a function of square of resonant frequency for tapered oxide and blunt oxide VCSELs

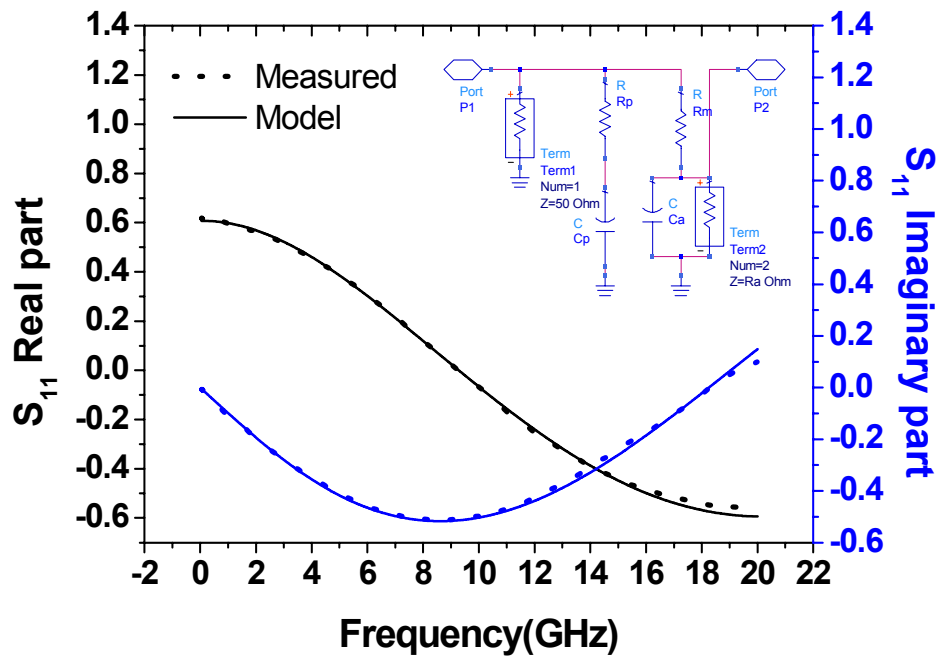
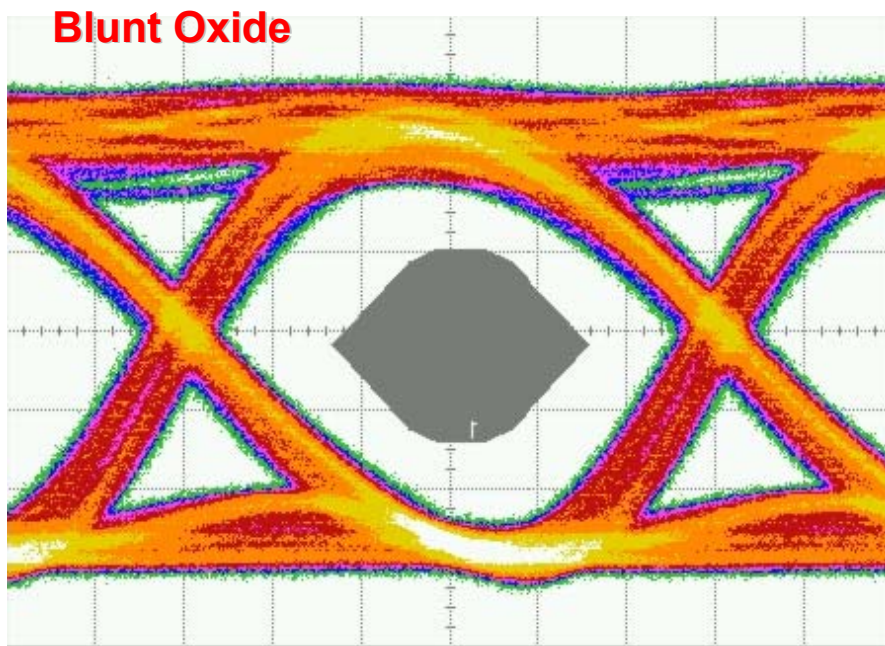
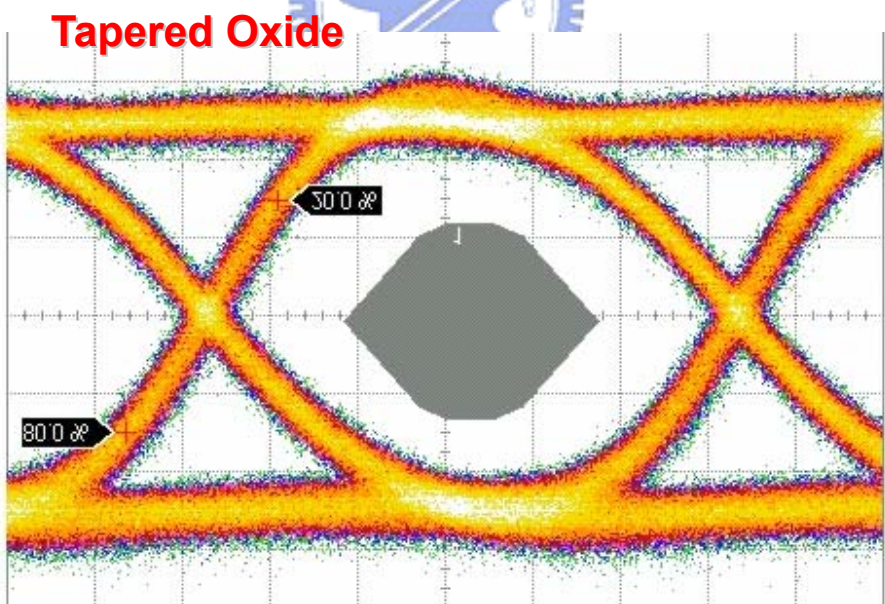


Figure 4-6 Real and imaginary S11 parameter versus frequency from model and measured data (dash line is measured data, solid line is simulated data)





(a) Blunt oxide VCSEL



(b) Oxide-implant VCSEL

Figure 4-7 Eye-diagram for tapered oxide and blunt oxide VCSELs

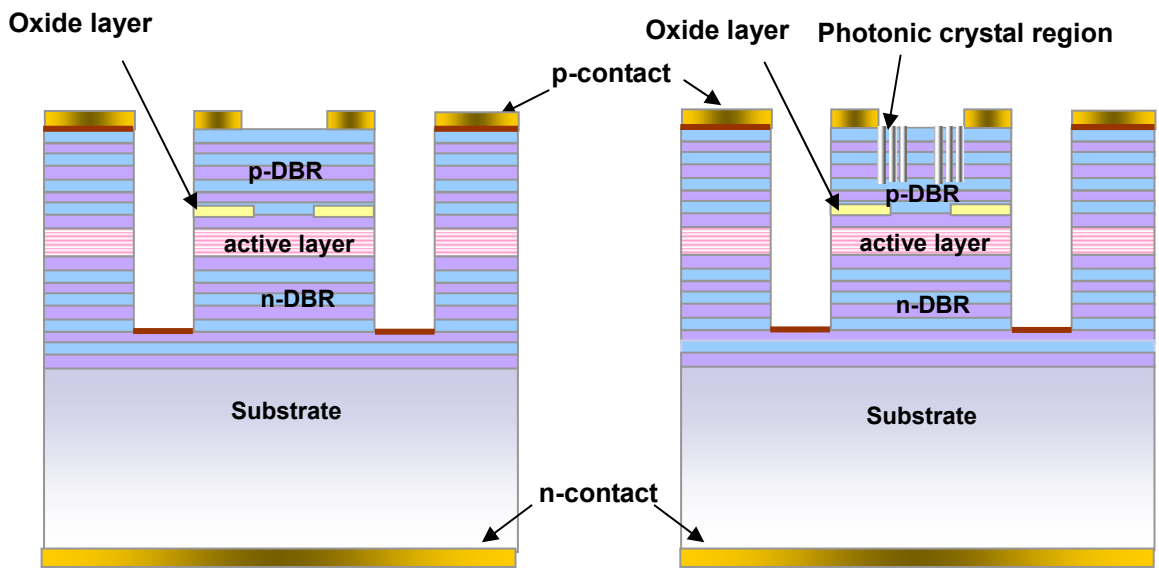


Figure 4-8 oxide VCSEL and oxide photonic crystal VCSEL structure



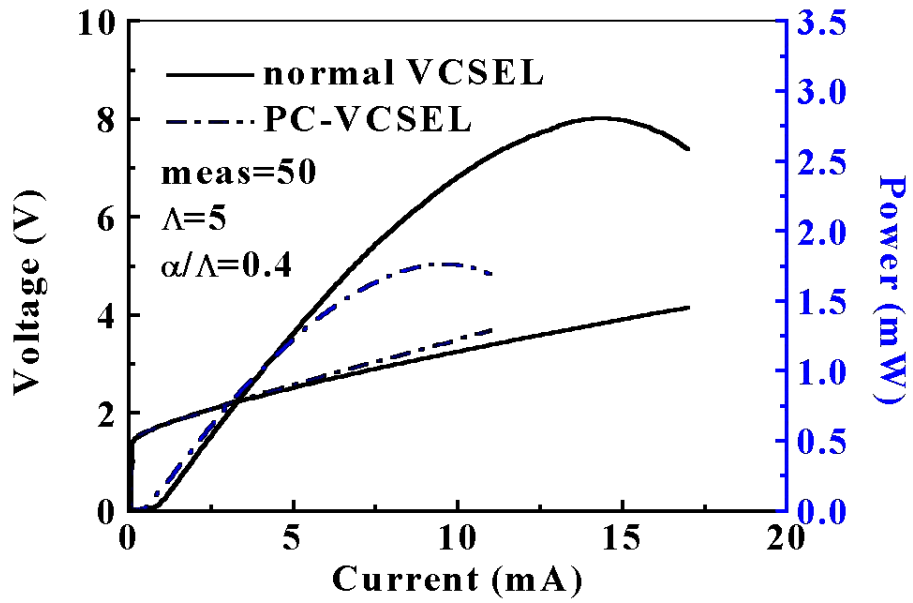


Figure 4-9 Typical LIV curve for oxide photonic crystal VCSELs

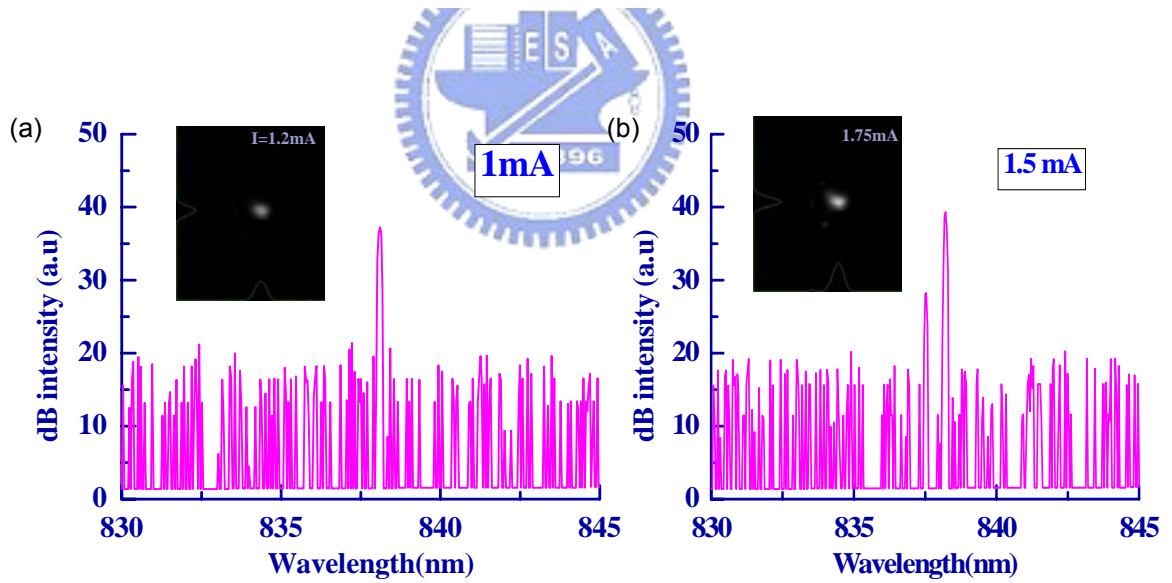


Figure 4-10 Spectral characteristics and near-field images for the photonic crystal VCSELs

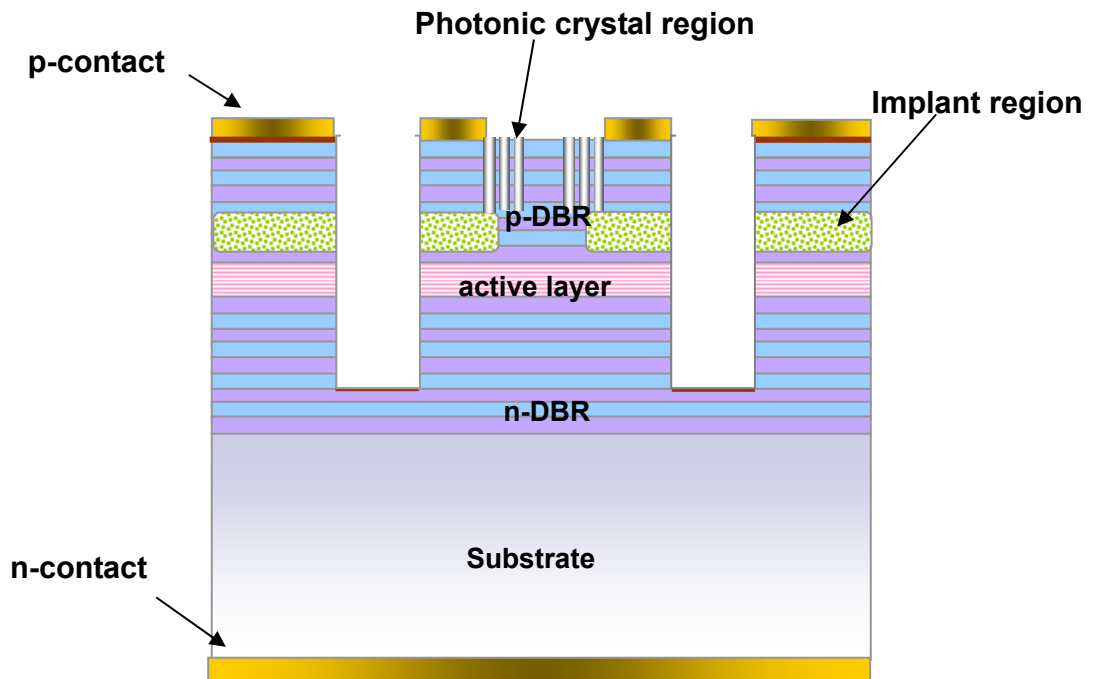


Figure 4-11 Implant photonic crystal VCSEL

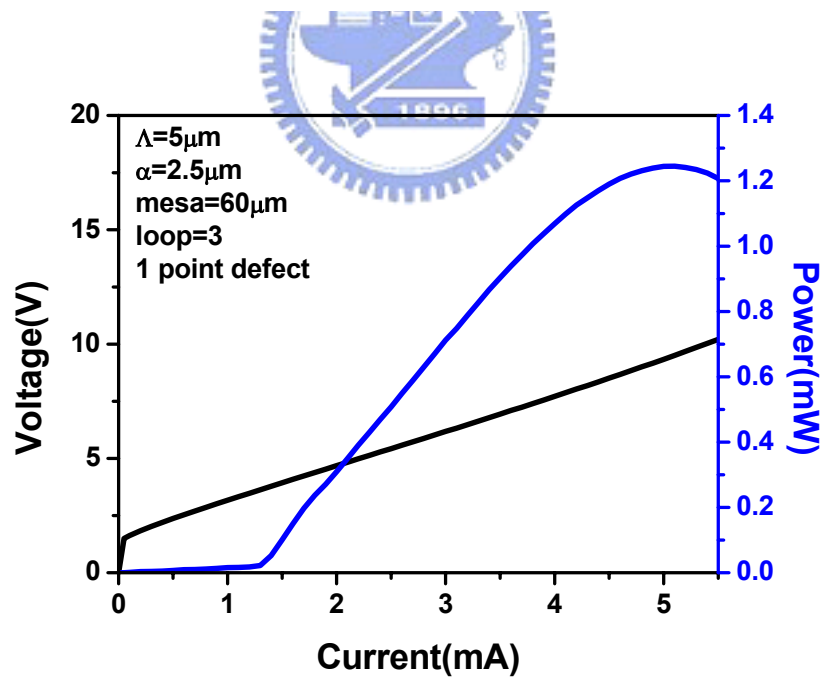


Figure 4-12 Typical LIV curve for implant photonic crystal VCSELs

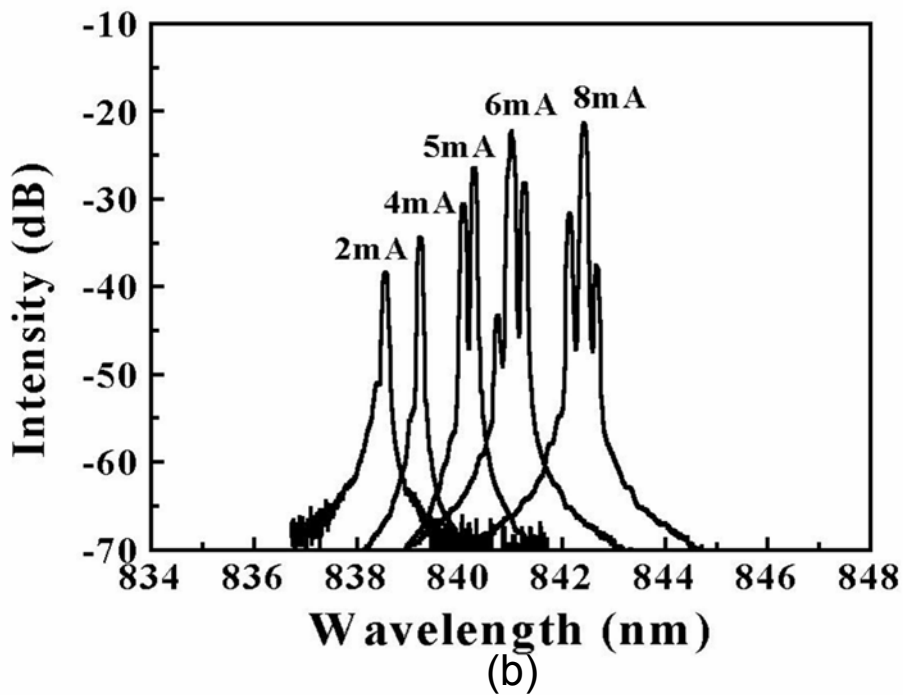
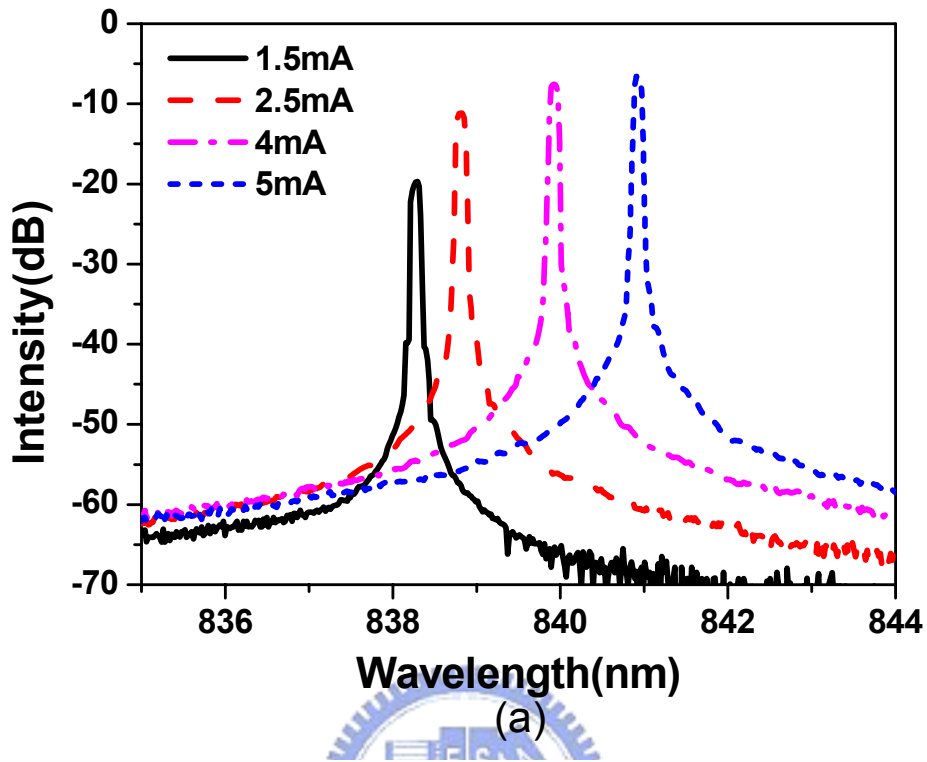


Figure 4-13 Spectral characteristics for the implant photonic crystal VCSELs and VCSEL without PC holes (a) PC-VCSEL (b)VCSEL

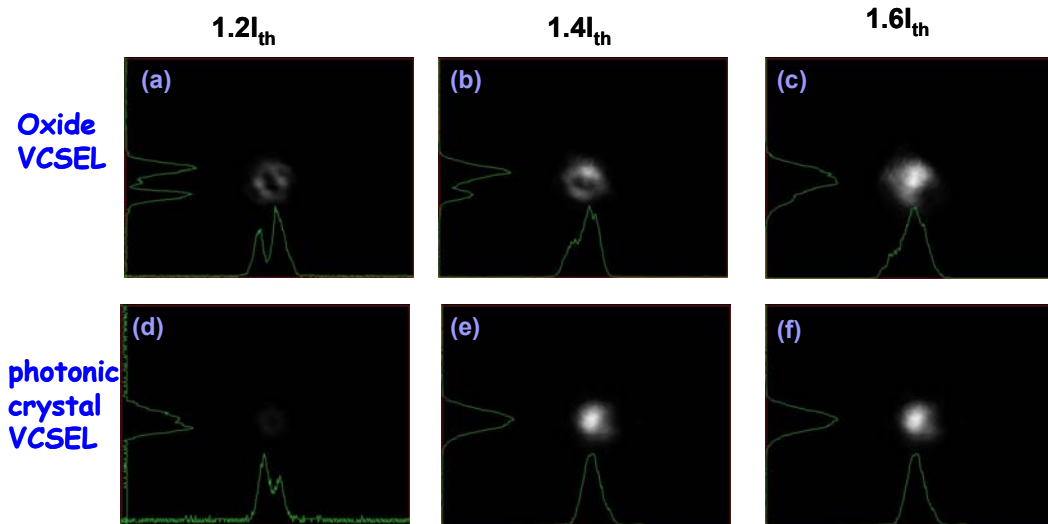


Figure 4-14 Far field patterns of the fimplant VCSELs observed under different drive currents are shown in (a)~(c) and the implant photonic crystal VCSEL are shown in (d)~(f)

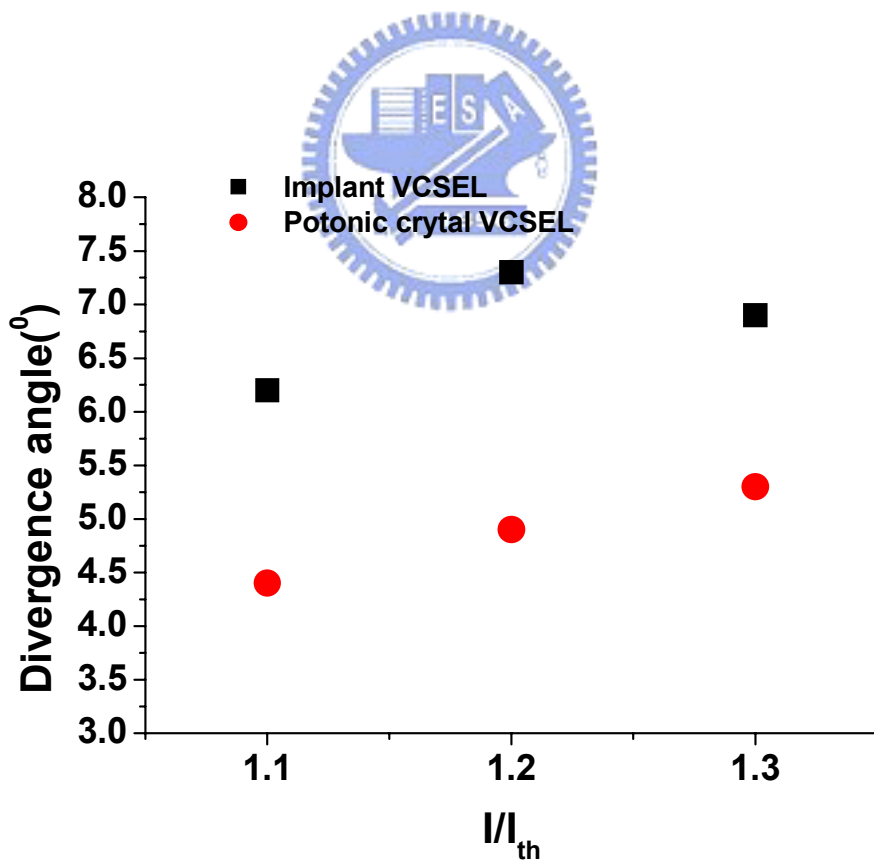


Figure 4-15 The divergence angle for implant and photonic crystal VCSELs

Tapered oxide VCSEL						
<i>Bias</i>	<i>L(nH)</i>	<i>Cp(pF)</i>	<i>Rp(Ω)</i>	<i>Rm(Ω)</i>	<i>Ra(Ω)</i>	<i>Ca(pF)</i>
0mA	0.25	0.16	4.98	63	1688	0.185
1mA	0.25	0.16	4.98	56	200	0.191
1.5mA	0.25	0.16	4.98	55	188	0.193
2mA	0.25	0.16	4.98	53	178	0.195
2.5mA	0.25	0.16	4.98	52	162	0.197
3mA	0.25	0.16	4.98	51	155	0.2
4mA	0.25	0.16	4.98	50	136	0.202
5mA	0.25	0.16	4.98	49	124	0.206
6mA	0.25	0.16	4.98	48	113	0.21
7mA	0.25	0.16	4.98	47	106	0.215
8mA	0.25	0.16	4.98	46	96	0.221
9mA	0.25	0.16	4.98	45	93	0.232
10mA	0.25	0.16	4.98	45	87	0.24

Table 4-1 Equivalent circuit elements at different bias current for Tapered oxide VCSEL

Chapter 5

Conclusion

We have performed experimental study of small signal modulation behavior of 850nm tapered oxide-implant and blunt oxide-implant VCSELs.

We have found that tapered oxides process gives VCSEL with excellent high speed performance without semi-isolating substrate. The damping rate from the modulation response was found to reduce two times in the tapered oxide VCSEL and therefore enhanced the maximal modulation bandwidth. With same oxide aperture size 5.5 μm , tapered oxide VCSEL shows better modulation bandwidth of 13.2 GHz while blunt oxide VCSEL has 9.5 GHz. A very clean eye was demonstrated from improved VCSEL with rising time of 26 ps, falling time of 40 ps and jitter of less than 20 ps, operating at 10Gb/s with 6mA bias and 6dB extinction ratio. We also build an equivalent circuit model to analyze the bandwidth limitation affected by VCSEL intrinsic impedance. The simulation results could make the modulation limitation clearly and help us to modify the VCSEL process for high speed operation.

In the second part of the thesis, we report a high power (>1 mW) singlemode proton-implanted photonic crystal vertical-cavity surface-emitting laser (PC-VCSEL) with high SMSR (> 40 dB) throughout the whole operation current range. This PC-VCSEL, with an aperture of about 10 μm , has ultra-low threshold current of about 1.25 mA. We analyze the L-I curve, emission spectra, near field pattern, divergence angles of photonic crystal VCSELs fabricated with oxide-confined and implant structure. The present results indicate that a VCSEL using proton implantation for

current confinement and photonic crystal for optical confinement is a reliable approach to achieve high-power singlemode operation of a VCSEL. This concept will be applied to a 1.3 μm VCSEL and other commercial applications in the future.



Reference

- [1] H. Soda, K. Iga, C. Kitahara, and Y. Suematsu, "GaInAsP/InP surface emitting injection lasers," Japanese Journal of Applied Physics, vol.18, pp.2329-2330, 1979.
- [2] K. Iga, F. Koyama, and S. Kinoshita, "Surface-emitting semiconductor lasers," IEEE Journal of Quantum Electronics, vol.24, pp.1845-1855, September 1988.
- [3] T. Honda, T. Shirasawa, N. Mochida, A. Inoue, A. Matsutani, T. Sakaguchi, F. Koyama, and K. Iga, "Design and fabrication processes consideration of GaN-based surface emitting lasers," Trans. IEICE, J81-C-II, pp.97-104, 1998.
- [4] "2003 年光電半導體產業及技術動態調查報告," PIDA, 2004.
- [5] R. Brand, "10 gigabit Ethernet interconnection with wide area networks," 10GEA, March 2003
- [6] G. P. Agrawal, *Fiber-Optic Communication Systems* ~Wiley, New York, 1997.
- [7] A. A. Maradudin and A. R. McGurn, J. Mod. Opt. 41, 275 ~1994.
- [8] J. D. Joannopoulos, R. D. Meade, and J. N. Winn, *Photonic Crystal- Molding the Flow of Light* ~Princeton University Press, Princeton, NJ,1995.
- [9] E. R. Hegblom, B. J. Thibeault, R. L. Naone, and L. A. Coldren, "Vertical cavity lasers with tapered oxide apertures for low scattering loss," *Electron. Lett.*, 33, pp. 869–879, 1997.
- [10] Yokouchi, N., Danner, A.J., and Choquette, K.D.: 'Etching depth dependence of the effective refractive index in two-dimensional photonic-crystal-patterned vertical-cavity surface-emitting laser structures', *Appl. Phys. Lett.*, 2003, 82, (9), pp. 1344–1346
- [11] A. Valle, J. Sarma, and K. A. Shore, "Spatial hole burning effects on the dynamics

of vertical cavity surface-emitting laser diodes,” *IEEE J.Quantum Electron.*, 31, pp. 1423–1431, 1995.

[12] Y. Liu, W.-C. Ng, B. Klein, and K. Hess, *IEEE J. QUANTUM ELECTRONICS*, **39**, 99-108 (2003)

[13] G. P. Agrawal and N. K. Dutta, “Semiconductor Lasers,” 2nd 276-280, Van Nostrand Reinhold published.

